

Laser spectroscopy of the lowlying electronic states of NbN: Electron spin and hyperfine effects in the states from the configurations $\sigma\delta$ and $\delta\pi$

Y. Azuma, G. Huang, M. P. J. Lyne, A. J. Merer, and V. I. Srdanov

Citation: *The Journal of Chemical Physics* **100**, 4138 (1994); doi: 10.1063/1.466298

View online: <http://dx.doi.org/10.1063/1.466298>

View Table of Contents: <http://scitation.aip.org/content/aip/journal/jcp/100/6?ver=pdfcov>

Published by the [AIP Publishing](#)

Articles you may be interested in

[Laserinduced Fluorescence Spectroscopy of NiS: Identification of a Lowlying Electronic State](#)

Chin. J. Chem. Phys. **26**, 140 (2013); 10.1063/1674-0068/26/02/140-144

[Theoretical characterization of the low-lying electronic states of NbC](#)

J. Chem. Phys. **123**, 054318 (2005); 10.1063/1.1978867

[Laser spectroscopy of NiI: Ground and low-lying electronic states](#)

J. Chem. Phys. **119**, 12245 (2003); 10.1063/1.1625921

[Laser spectroscopy of NiBr: Ground and low-lying electronic states](#)

J. Chem. Phys. **117**, 3694 (2002); 10.1063/1.1494777

[On the lowlying electronic states of the molecule BeN](#)

J. Chem. Phys. **95**, 9086 (1991); 10.1063/1.461187



Laser spectroscopy of the low-lying electronic states of NbN: Electron spin and hyperfine effects in the states from the configurations $\sigma\delta$ and $\delta\pi$

Y. Azuma,^{a)} G. Huang, M. P. J. Lyne, A. J. Merer, and V. I. Srdanov^{b)}

Department of Chemistry, University of British Columbia, 2036 Main Mall, Vancouver, British Columbia V6T 1Z1, Canada

(Received 08 September 1993; accepted 29 November 1993)

Rotational and hyperfine analyses have been carried out for the (0,0) bands of the $C^3\Pi-X^3\Delta$, $e^1\Pi-X^3\Delta$, and $f^1\Phi-a^1\Delta$ transitions of gaseous NbN from laser excitation spectra taken at sub-Doppler resolution. The $\delta\pi$ $C^3\Pi$ and $e^1\Pi$ states lie only 102 cm^{-1} apart in zero order but the spin-orbit matrix element between them, which is the sum of the spin-orbit constants for the δ and π electrons, is 698 cm^{-1} ; as a result the $^3\Pi_1$ spin component lies below both the $^3\Pi_0$ and $^3\Pi_2$ components, and its hyperfine structure is highly irregular. This irregularity is an extreme example of how cross terms between the spin-orbit interaction and the Fermi contact hyperfine operator alter the apparent value of the hyperfine a constant, the coefficient of $\mathbf{I} \cdot \mathbf{L}$ in the magnetic hyperfine Hamiltonian. Molecular parameters for the $C^3\Pi$ and $e^1\Pi$ states have been obtained from a combined fit to the two of them. Including data for the $B^3\Phi$ state recorded earlier [Azuma *et al.*, J. Chem. Phys. **91**, 1 (1989)], detailed information is now available for all six of the electronic states from the electron configurations $\sigma\delta$ and $\delta\pi$. It has been verified that the spin-orbit/Fermi contact cross terms cause roughly equal and opposite shifts in the hyperfine a constants for the singlet states and the $\Sigma=0$ components of the triplet states. After allowing for this effect, it has been possible to interpret the hyperfine a constants in terms of one-electron parameters for the δ and π electrons, in similar fashion to spin-orbit parameters. Wavelength resolved fluorescence, following selective laser excitation of the $C^3\Pi$, $e^1\Pi$, and $f^1\Phi$ states, has led to the discovery of three new electronic states, $\delta^2 c^1\Gamma$, $\delta^2 d^1\Sigma^-$, and $\sigma^2 b^1\Sigma^+$, besides giving the absolute position of $a^1\Delta$. Strong configuration interaction mixing is found to occur between the $\sigma^2 b^1\Sigma^+$ and $\delta^2 d^1\Sigma^+$ states. The low-lying electronic states of NbN are now well understood.

I. INTRODUCTION

The nuclear hyperfine structure of compounds of niobium is particularly impressive because the only stable isotope, ^{93}Nb , has a spin $I=9/2$ and possesses the largest magnetic moment of any nonradioactive nucleus. The low-lying electronic states of NbN¹⁻⁴ are well described by the single configuration approximation, and are not perturbed rotationally; they provide "textbook" examples of hyperfine structure in open shell molecules. Since the hyperfine constants are related to expectation values of the electron coordinates relative to the spinning nuclei, the hyperfine structures of Nb compounds, such as NbN, can provide exacting tests of the quality of *ab initio* wave functions and of models of chemical bonding; as yet the challenge for these metal compounds has not been taken up by the theoreticians.

The $B^3\Phi-X^3\Delta$ system of NbN, near 6000 \AA , illustrates⁴ how the hyperfine structure of a multiplet case (a) electronic state can be expected to behave in the general case. The normal pattern for a regular triplet state (where the spin-orbit coupling is positive) turns out to be that the

energy order of the hyperfine components reverses at quite low J values in the outer two spin components. Another important effect is spin-orbit distortion of the hyperfine structure, which is needed to account for the departures from the expected case ($a_{\beta\beta}$) hyperfine energy expressions in the $X^3\Delta$ state. It arises as a second-order cross term between the Fermi contact and spin-orbit operators, and causes equal and opposite shifts for singlet and triplet states in the apparent hyperfine a parameter, the coefficient of $\mathbf{I} \cdot \mathbf{L}$ in the magnetic hyperfine Hamiltonian.⁵

The hyperfine structure in the $B^3\Phi-X^3\Delta$ system of NbN could not have been interpreted⁴ without information on the spin-orbit couplings and the position of the low-lying $a^1\Delta$ state. The spin-orbit couplings are not directly measurable in the $B^3\Phi-X^3\Delta$ transition because both states are in good case (a) coupling, and only $\Delta\Sigma=0$ branches appear.⁶ The present paper follows on from Ref. 4. It describes the $C^3\Pi-X^3\Delta$ transition, where the smaller spin-orbit coupling of the $C^3\Pi$ state allows the spin-orbit intervals to be obtained from laser measurements of $\Delta\Sigma\neq 0$ spin-satellite branches. It also reports the discovery of five new electronic states, including the $a^1\Delta$ state. Unexpected new effects were again encountered: the $C^3\Pi$ state has an abnormal energy order for its triplet spin components because of exceptionally strong mixing with the $e^1\Pi$ state from the same electron configuration, and there is evidence

^{a)}Present address: Physics Division, Argonne National Laboratory, 9700 South Cass Avenue, Argonne, Illinois 60439.

^{b)}Present address: Department of Chemistry, University of California at Santa Barbara, Santa Barbara, California 93106.

for strong configuration interaction between the $^1\Sigma^+$ states from the configurations σ^2 and δ^2 . Sub-Doppler hyperfine data are now available for all six states from the electron configurations $\sigma\delta$ and $\delta\pi$; it is shown that the hyperfine a constants, after correction for the spin-orbit distortion, can be interpreted in terms of one-electron parameters, just as spin-orbit constants can be related to one-electron parameters. NbN continues to provide beautiful examples of new hyperfine effects in open shell molecules.

II. EXPERIMENTAL DETAILS

Gaseous niobium nitride (Nb^{14}N) was prepared in a flow system by reacting NbCl_5 vapor with a trace of active nitrogen in a 2450 MHz microwave discharge operating at 100 W power. The NbCl_5 vapor was produced by sublimation of NbCl_5 powder, contained in the sidearm of a quartz tube, at about 80 °C; it was then entrained in a mixture of N_2 and Ar carrier gas and passed through the microwave cavity. The microwave discharge produced a 10-cm long lavender-colored flame, which was pumped across a stainless steel fluorescence cell fitted with Brewster-angle windows and light baffles. The total gas pressure in the cell was maintained at between 0.3 and 1 Torr. We found that, within this pressure range, high pressure favored the production of NbN in its ground electronic state, while low pressure enhanced the production of molecules in the low-lying excited states. Studies of the NbN spectrum were carried out in the visible region by laser excitation and in the near infrared by wavelength-resolved fluorescence.

The laser employed was a Coherent Inc. model 599-21 standing wave tunable dye laser, pumped by a Coherent Inc. model Innova 90-6 argon ion laser. Typical output power from the dye laser was in the range 15–150 mW, depending on the spectral region and the laser dye used. Doppler-limited excitation spectra were recorded in the region 14 500–18 500 cm^{-1} using the dyes DCM, rhodamine 590, and rhodamine 560. Sub-Doppler spectra were also recorded in selected regions using the technique of intermodulated fluorescence.⁷ The linewidth was typically 750 MHz for the Doppler-limited spectra and 100 MHz for the sub-Doppler spectra. The excitation spectra were recorded as 35 GHz continuous scans of laser frequency under the control of a MicroVAX computer; the controlling program also acquired the iodine excitation spectrum and the fringe patterns (interpolation markers) from a 299 MHz free spectral range Fabry-Perot interferometer to provide calibration. Successive scans over a 10 cm^{-1} region were concatenated and the frequencies of the I_2 lines in the region, taken from Gerstenkorn and Luc's iodine atlas,⁸ were fitted to a linear expression in the marker positions to derive the frequency of the first marker and the exact free spectral range of the etalon; this was then used to convert the marker positions of the NbN lines to absolute frequencies. Although the frequency of an individual I_2 line has an uncertainty of $\pm 0.0025 \text{ cm}^{-1}$ because of unresolved quadrupole structure, our calibration method produces consistent line frequencies with relative precisions of $\pm 0.0003 \text{ cm}^{-1}$ for the sub-Doppler lines, be-

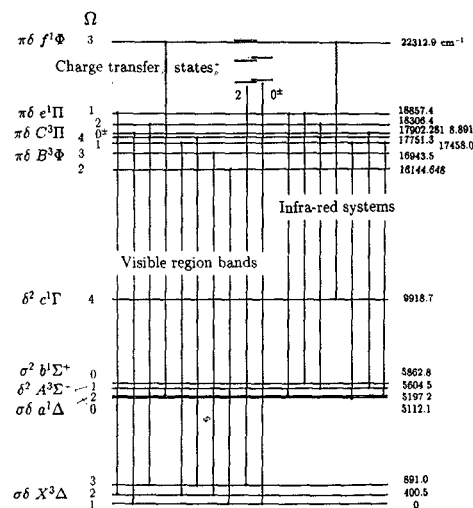


FIG. 1. Electronic states and transitions of NbN, as presently known.

cause it averages over all the iodine lines in the region of interest.

In the wavelength-resolved fluorescence studies of the near-infrared electronic transitions we excited selected lines of the band systems in the visible, and focused the fluorescence through a pair of lenses onto the entrance slit of a 0.75 m spectrometer (Spex model 1702). The dispersed fluorescence was then detected with a microchannel plate-intensified array detector (PAR model 1461) mounted in place of the exit slit of the spectrometer. In the near-infrared region, the spectral width of the detector is about 150 Å, with a resolution of about 0.5 cm^{-1} . The fluorescence spectra were taken with exposure times ranging from a few seconds for strong NbN lines to half a minute for weak spectral features. The whole process from data acquisition to spectral calibration was performed under the control of a PDP 11/23 minicomputer.

Calibration of the resolved fluorescence spectra was provided by emission lines from an iron–neon hollow cathode lamp recorded in the same spectral window. The vacuum wavelengths of the Fe and Ne atomic lines, taken from Crosswhite's tables,⁹ were fitted to a three-term polynomial to obtain the calibration constants. The accuracy of the calibrated spectral lines is limited by the characteristics of the array detector to about $\pm 0.2 \text{ cm}^{-1}$.

III. AN OVERVIEW OF THE ELECTRONIC STATES AND TRANSITIONS OF NbN

Until recently, the only known electronic transitions of NbN were the $B^3\Phi-X^3\Delta$ and $C^3\Pi-X^3\Delta$ systems, which dominate the absorption and emission spectra in the visible region.^{1–3} The present detailed analysis of the laser excitation spectra in the visible region and the wavelength-resolved fluorescence spectra in the infrared region has revealed many more new electronic transitions. Figure 1 shows the electronic states and transitions of NbN known to this date. Analyses of most of the new transitions are reported in this paper, though studies of the charge-

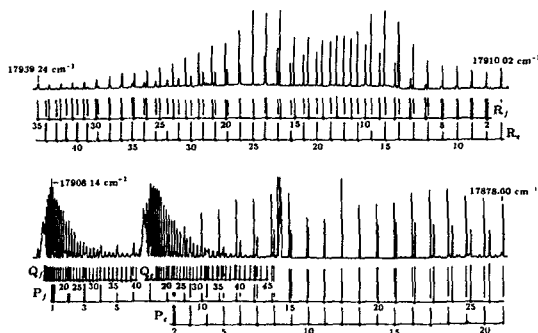


FIG. 2. The $C^3\Pi_0-X^3\Delta_1(0,0)$ subband of NbN at Doppler-limited resolution. The subscript letters in the branch labels are the upper state parities.

transfer transitions and the extensive vibrational hot bands of the $B-X$ and $C-X$ systems will be reported elsewhere. In the following sections, we present detailed analyses of the spin and hyperfine structure of the $C-X$ system, the hyperfine structure of the $e-X$ and $f-a$ systems, and rotational analysis of the infrared systems.

IV. ANALYSIS OF THE $C^3\Pi-X^3\Delta$ SYSTEM NEAR 5600 Å

A. The rotational structure

The $C^3\Pi-X^3\Delta$ system of gaseous NbN occurs in the region 17 000–18 000 cm^{-1} . At low resolution, the spectrum appears as three short red-degraded vibrational sequences which result from the triplet spin multiplicity. The strongest subbands, as observed in laser excitation, are the $^3\Pi_0-^3\Delta_1(0,0)$ subband at 17 905 cm^{-1} and the $^3\Pi_2-^3\Delta_3(0,0)$ subband at 17 415 cm^{-1} . The system is far from normal since the “central” $^3\Pi_1-^3\Delta_2(0,0)$ subband does not lie halfway between the other two, but appears at 17 057 cm^{-1} ; also it has only about half their intensity. In fact its assignment remained in doubt for some time. The subbands of the $C-X$ system possess single R , Q , and P branches, except for the $^3\Pi_0-^3\Delta_1$ subband near 17 905 cm^{-1} , which is illustrated in Fig. 2. This subband consists of two sets of red-degraded R , Q , and P branches, with Q heads at 17 902 and 17 908 cm^{-1} , as a result of the Λ doubling in the $^3\Pi_0$ upper state, which in first approximation is independent of J . The Λ doubling in the other $^3\Pi$ substates is much smaller and is not observed at Doppler-limited resolution except at the highest J values. The par-

ities of the two $C^3\Pi_0$ levels have now been established (see Sec. IX A) as e for the upper state of the 17 902 cm^{-1} subband and f for the upper state of the 17 908 cm^{-1} subband. The branch intensity patterns in the $C-X$ transition are characteristic for a $\Delta\Lambda = -1$ transition: a strong Q branch, a moderately strong P branch, and a relatively weak R branch. In most of the branches, the rotational lines are well separated and can be followed to about $J=50$. The only unresolved rotational structure in the spectra occurs in the dense Q heads where the small rotational line separation compared to the large hyperfine width causes successive rotational lines to overlap. Since the R and P branches are well resolved in the low J regions, they can be followed down to their first lines, and give the Ω values of the combining states. The relative branch intensities calculated for these Ω values from the Hönl-London factors¹⁰ are consistent with what is observed. A set of effective rotational constants for the $^3\Pi$ and $^3\Delta$ states has been derived from the relatively narrow high J rotational lines; these are given in Table I. The positions of the assigned rotational lines of the $^3\Pi-^3\Delta$ system are listed in the Ph.D. thesis of one of us (G.H.).

B. The spin-orbit structures of the $X^3\Delta$ and $C^3\Pi$ states

From the origins of the three $C-X(0,0)$ subbands given in Table I, it is clear that the spin structure of the $C-X$ system is anomalous, with the $^3\Pi_1-^3\Delta_2$ subband shifted down from its expected position by 603 cm^{-1} . The reason for this large shift is that the $X^3\Delta$ and $C^3\Pi$ states both interact strongly with singlet states from their respective electron configurations. Obviously, in order to understand the details of the interactions, a direct measurement of the spin-orbit intervals is needed. In the present case this is not easy to achieve because of the good Hund's case (a) spin coupling in all the degenerate states of NbN, which has the effect that the spin satellite branches of the $B^3\Phi-X^3\Delta$ and $C^3\Pi-X^3\Delta$ systems are too weak to be observed in regular absorption or emission spectra.

A determination of the spin-orbit intervals in the $X^3\Delta$ ground state of NbN had been attempted by Pazyuk *et al.* following a rotational analysis of the absorption spectrum in the region 560–670 nm.² However, the reported spin-orbit parameters were erroneous since the two subbands assigned by Pazyuk *et al.* as the $B^3\Phi_3-X^3\Delta_3$ and $B^3\Phi_2-X^3\Delta_2$ spin satellites, and used by them to calculate the spin-orbit intervals, are actually the $^3\Pi_1-^3\Delta_2$ and $^3\Pi_2-^3\Delta_3$

TABLE I. Rotational constants from the $C^3\Pi-X^3\Delta(0,0)$ subbands of NbN.^a

Subband	ν_0	B'_{eff}	$10^7 D'_{\text{eff}}$	B''_{eff}	$10^7 D''_{\text{eff}}$
$^3\Pi_0-^3\Delta_1$	17 902.281(3)	0.496 47(9)	5.08(42)	0.500 13(9)	4.58(42)
$^3\Pi_0-^3\Delta_1$	17 908.891(3)	0.496 57(9)	5.13(45)	0.500 14(9)	4.68(45)
$^3\Pi_1-^3\Delta_2$	17 057.474(1)	0.495 30(2)	4.98(15)	0.501 73(2)	4.69(15)
$^3\Pi_2-^3\Delta_3$	17 415.443(12)	0.496 19(9)	5.06(24)	0.502 53(9)	4.72(27)

^aAll values in cm^{-1} , with error limits of three standard deviations. The energy expression used contained no terms in Ω , so that ν_0 is the hypothetical $Q(0)$ line position. The standard deviations σ of the least squares fits were about 0.0017 cm^{-1} .

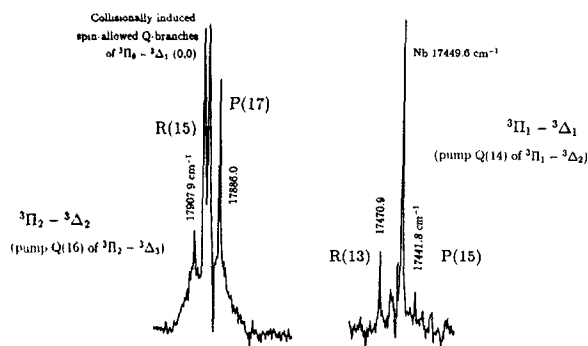


FIG. 3. Spin satellite branches of the $C^3\Pi-X^3\Delta$ system of NbN, recorded as wavelength-resolved fluorescence following laser excitation of (a) the $C^3\Pi_2-X^3\Delta_3$ (0,0) subband and (b) the $C^3\Pi_1-X^3\Delta_2$ (0,0) subband.

subbands of the $C-X$ system. In 1988, Féménias *et al.*³ estimated the spin-orbit intervals in the ground state from the effective rotational constants of the three $X^3\Delta$ components using Mulliken's formula,⁶ though because of the approximate nature of this formula their estimate can only be good to about 15%. In what follows, we report observations of two of the $\Delta\Sigma \neq 0$ spin satellites of the $C-X$ system using the sensitive method of wavelength-resolved fluorescence, following laser excitation of selected lines of the allowed subbands.

The strength of a spin-satellite transition depends on how different the spin coupling is in the two combining electronic states, with the strongest satellites being observed when one of the states is in case (a) coupling and the other in case (b). All electronic states in case (a) coupling uncouple towards case (b) to some extent with increasing rotation, with the degree of spin uncoupling for given J being inversely proportional to the spin-orbit coupling constant A . The spin-orbit intervals in the known states of NbN are comparatively large, so that the amount of spin uncoupling is not great, but the smallest spin-orbit coupling occurs in the $C^3\Pi$ state, so that the chances of observing spin satellite lines are greatest in the $C^3\Pi-X^3\Delta$ transition.

Figure 3 shows the fluorescence patterns obtained following laser excitation of the case-(a)-allowed components of the $^3\Pi-^3\Delta$ transition. In Fig. 3(a), the laser excites the $Q(16)$ rotational line of the $^3\Pi_2-^3\Delta_3$ subband. About 500 cm^{-1} to the blue of the exciting line, two sharp fluorescence lines are observed; these are the $R(15)$ and $P(17)$ lines of the $^3\Pi_2-^3\Delta_2$ spin-satellite transition. There is no doubt about the line assignments since the line separation agrees with the combination difference of the $X^3\Delta_2$ substate to within experimental error. The weak $Q(16)$ line is unfortunately buried under the strong collision-induced features between the R and P lines, and is not observed. The strong doublet feature at the center of Fig. 3(a), and the broad structure underneath the sharp R and P rotational lines, represent the unresolved R , Q , and P branches of the $^3\Pi_0-^3\Delta_1$ transition, appearing as a result of collisional energy transfer. The doubled Q branch results from

the Λ doubling in the $C^3\Pi_0$ substate, as discussed above. Figure 3(b) shows the $R(13)$ and $P(15)$ rotational lines of the $^3\Pi_1-^3\Delta_1$ spin-satellite transition, induced by laser excitation of the $Q(14)$ line of the $^3\Pi_1-^3\Delta_2$ subband. As expected for a $\Delta\Omega=0$ parallel transition, the spin-satellite $Q(14)$ line is weak; in our spectra it is also blended with a Nb atomic line.

By comparing the positions of the spin-satellite lines measured from Fig. 3 with those of the corresponding rotational lines of the spin-allowed $^3\Pi-^3\Delta$ subbands, we could obtain the $^3\Delta_2-^3\Delta_1$ and $^3\Delta_3-^3\Delta_2$ separations. If the rotational energy of a given Ω substate is taken as

$$E(J) = T_\Omega + B_\Omega J(J+1) - D_\Omega [J(J+1)]^2, \quad (1)$$

where the B_Ω and D_Ω values are given in Table I, we find the ground state spin-orbit intervals for zero rotation to be

$$\Delta E(^3\Delta_2-^3\Delta_1) = 400.5 \pm 0.1 \text{ cm}^{-1}; \quad (2)$$

$$\Delta E(^3\Delta_3-^3\Delta_2) = 490.5 \pm 0.1 \text{ cm}^{-1}.$$

The subband origins of the $C-X$ (0,0) transition (Table I) then give the energies of the spin-orbit components of the $C^3\Pi$ state, relative to $X^3\Delta_1$ as zero, as

$$\begin{aligned} T(C^3\Pi_2) &= 18\,306.4 \pm 0.1 \text{ cm}^{-1}, \\ T(C^3\Pi_1) &= 17\,458.0 \pm 0.1 \text{ cm}^{-1}, \\ T(C^3\Pi_{0f}) &= 17\,908.891 \pm 0.003 \text{ cm}^{-1}, \\ T(C^3\Pi_{0e}) &= 17\,902.281 \pm 0.003 \text{ cm}^{-1}. \end{aligned} \quad (3)$$

Equations (2) and (3) show that the middle components of the $X^3\Delta$ and $C^3\Pi$ states have been shifted down, from their first-order positions, by about 45 and 650 cm^{-1} , respectively. It was shown in Ref. 4 that the asymmetric spin structure in the X state is caused by second-order spin-orbit interaction with the $a^1\Delta$ state from the same electron configuration, $\sigma\delta$. Likewise the distorted spin structure of the C state must result from a similar kind of perturbation by the $e^1\Pi$ state of the $\delta\pi$ electron configuration. The unusually great displacement of the $^3\Pi_1$ substate from its first-order position suggests an extremely large second-order spin-orbit interaction between the $C^3\Pi_1$ and $e^1\Pi$ states, and therefore a heavy mixing of the two states. Consequently, the oscillator strength is shared between the $C^3\Pi_1-X^3\Delta_2$ and $e^1\Pi-X^3\Delta_2$ transitions. Since the $e-X$ intercombination system has no oscillator strength in zero order, the mixing weakens the $C^3\Pi_1-X^3\Delta_2$ transition and causes the $e-X$ transition to become observable.

C. The hyperfine structure

In order to study the hyperfine structure of the $C^3\Pi$ state, we recorded sub-Doppler spectra of parts of the (0,0) vibrational band of the $C^3\Pi-X^3\Delta$ transition by intermodulated fluorescence. Our sub-Doppler spectra cover the region of the dense Q branches and the low- J R and P lines; in the latter the hyperfine structure is well resolved and allows precise measurement of the line positions. The Q heads of the three $^3\Pi-^3\Delta$ (0,0) subbands are shown at

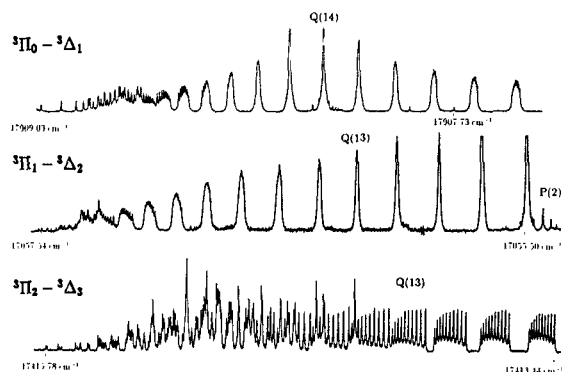


FIG. 4. Q heads of the $C^3\Pi-X^3\Delta$ (0,0) band of NbN at sub-Doppler resolution, illustrating the evolution of the hyperfine patterns with J . The upper trace is the $C^3\Pi_0-X^3\Delta_1$ component; hyperfine components of the $R_e(4)$ and $P_f(1)$ lines are also present. Each trace covers about 2 cm^{-1} .

sub-Doppler resolution in Fig. 4. The $^3\Pi_2-^3\Delta_3(0,0)$ subband shows considerably larger hyperfine splittings than the other two subbands, with all the hyperfine components of a rotational transition clearly resolved. For the $^3\Pi_0-^3\Delta_1$ and $^3\Pi_1-^3\Delta_2$ subbands, the hyperfine splittings decrease so rapidly with increasing J that the hyperfine structure is only resolved to about $J=10$. In the $^3\Pi_0-^3\Delta_1(0,0)$ subband, the rotational linewidth passes through a minimum at $J \approx 14$, and then widens with increasing rotation. After $J=20$, the hyperfine lines are resolved again but with a reversed hyperfine pattern. The hyperfine structure of the $^3\Pi_1-^3\Delta_2(0,0)$ subband never becomes resolved at higher J , though its width is not zero. Beyond about $J=30$ the Λ doubling becomes comparable to the hyperfine width, which results in some confused patterns.

The lines near $J=14$ in the $^3\Pi_0-^3\Delta_1$ subband are narrow and very intense because all the hyperfine components lie at the same position, which produces a series of sharp “spikes.” This spiking is a spin-uncoupling effect in the $X^3\Delta$ state, which was described in Ref. 4, and is also seen in the corresponding transition of VN.¹¹ Briefly, it occurs because the $X^3\Delta$ state is “regular” (with a positive value for A , the spin-orbit coupling constant) and also has a large Fermi contact parameter. The diagonal matrix element of the Fermi contact interaction includes a factor Σ in case (a) coupling, while it is proportional to $J-N$ in case (b).¹² The correlation between case (a) and case (b) for a regular triplet state is

$$\Sigma = 1 \leftrightarrow F_1(J=N+1); \quad \Sigma = -1 \leftrightarrow F_3(J=N-1)$$

so that with increasing rotation the negative Fermi contact interaction of $^3\Delta_1(\Sigma=-1)$ must turn into the positive Fermi contact interaction of F_3 . The rapidity with which this occurs was discussed in Ref. 11. Since the hyperfine widths are much larger in the $^3\Delta$ state than in the $^3\Pi$ state, it is the changing hyperfine patterns in the $^3\Delta$ state that cause the spiking observed in the $^3\Pi_0-^3\Delta_1$ subband. Spiking is also seen in the $^3\Pi_2-^3\Delta_3$ subband, although it occurs at a much higher J value, near 38. Since the hyperfine splitting in the middle component of a triplet state is much smaller

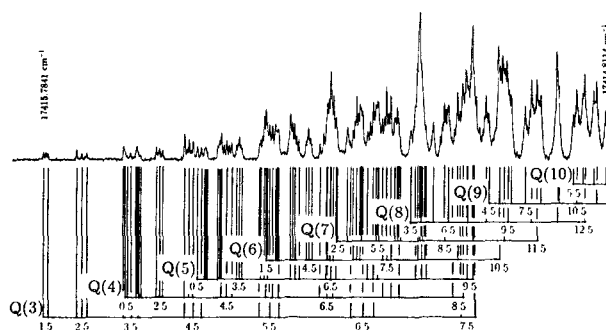


FIG. 5. Line assignments in the Q head of the $C^3\Pi_2-X^3\Delta_3$ (0,0) subband of NbN.

than those in the other two components, and less sensitive to rotation, the hyperfine patterns in the $^3\Pi_1-^3\Delta_2$ subband do not change significantly with J .

The assignment of the hyperfine F quantum numbers is easy for the clearly resolved and well-separated R and P lines because the hyperfine line positions go as $F(F+1)$. The hyperfine components therefore open out on the high F side; also the higher F lines have greater intensity. The hyperfine structure in the Q branches follows the same pattern, but the small rotational spacings mean that overlapping of the hyperfine structure is very extensive near the bandheads; the lines can only be assigned by matching the observed and calculated transition frequencies. The assignments in the crowded Q heads of the $^3\Pi_2-^3\Delta_3$ (0,0) and $^3\Pi_0-^3\Delta_1$ (0,0) subbands are shown in Figs. 5 and 6. A few $\Delta F \neq \Delta J$ lines can be seen in the Q head of the $^3\Pi_2-^3\Delta_3$ (0,0) subband, but many more appear in the low- J P lines illustrated in Fig. 7. No $\Delta F \neq \Delta J$ transitions are found in the $^3\Pi_0-^3\Delta_1$ (0,0) Q head, and those few that appear in the low- J P lines have no crossover resonances (see Fig. 8). This means that the hyperfine splitting in the upper state is very small, presumably because of the factor $\Omega=0$ in the diagonal matrix element of the magnetic hyperfine Hamiltonian, so that the $\Delta F \neq \Delta J$ transitions lie at exactly the same positions as the $\Delta F = \Delta J$ transitions sharing the same lower levels.

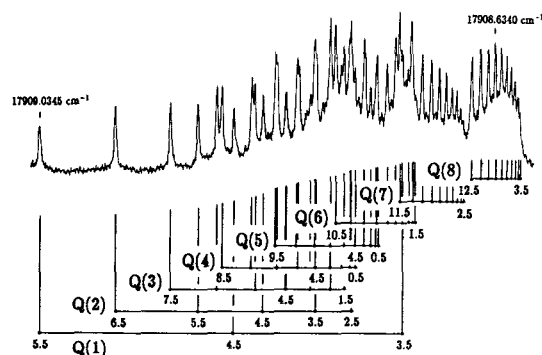


FIG. 6. Line assignments in the Q head of the $C^3\Pi_0-X^3\Delta_1$ (0,0) subband of NbN. Unlike Fig. 5, no hyperfine satellites ($\Delta F \neq \Delta J$) are observed because of the near zero hyperfine splittings in the upper state.

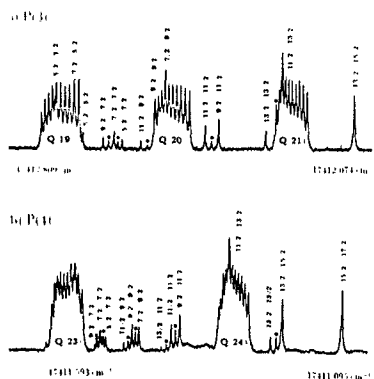


FIG. 7. (a) $P(3)$ and (b) $P(4)$ lines of the $C^3\Pi_2-X^3\Delta_3$ (0,0) subband of NbN at sub-Doppler resolution, illustrating the appearance of the hyperfine structure. Crossover resonances are marked with dots.

Since the $^3\Pi_1-^3\Delta_2$ (0,0) subband is weaker, and the signal-to-noise ratio is correspondingly lower, the hyperfine structure of the Q branch at low J is only partially resolved. However some low- J P lines are clearly resolved and show some interesting hyperfine patterns; Fig. 9 shows the assigned hyperfine structure of the first three P lines of the $^3\Pi_1-^3\Delta_2$ subband. In these lines the $\Delta F = \Delta J$ and the $\Delta F \neq \Delta J$ components are separated into two groups with the $\Delta F = \Delta J$ transitions on the low frequency side; the ordering of the $\Delta F = \Delta J$ hyperfine components of the $P(2)$ line is such that the high F component lies at the high frequency side, but the order reverses at higher J . A similar reversal was described in Ref. 4.

V. THE STRUCTURE OF THE $e^1\Pi-X^3\Delta_2$ TRANSITION

As indicated in Sec. IV B, the $e^1\Pi$ electronic state is quite heavily mixed with the $C^3\Pi_1$ state, such that enough intensity is transferred from the $C-X$ system to the $e-X$ intercombination system to make it appear in the excitation spectrum. The $e^1\Pi-X^3\Delta_2$ (0,0) band was weaker than we expected, judging by the amount of intensity lost from the $C^3\Pi_1-X^3\Delta_2$ bands but, after much searching,

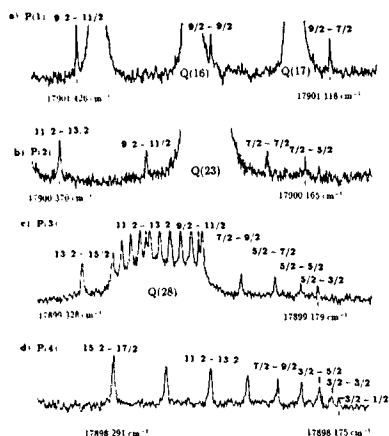


FIG. 8. The hyperfine patterns of the first four P lines of the $C^3\Pi_{0e}-X^3\Delta_1$ (0,0) subband of NbN. As in Fig. 6 no hyperfine satellites ($\Delta F \neq \Delta J$) are observed because of the near zero hyperfine splittings in the upper state.

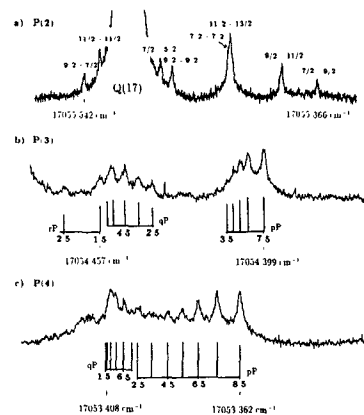


FIG. 9. The lines $P(2)$ – $P(4)$ in the $C^3\Pi_1-X^3\Delta_2$ (0,0) subband of NbN, showing how the hyperfine components are grouped according to the different ΔF selection rules.

was found at $18\,457\text{ cm}^{-1}$ (Q head). Its branch structure is like that of the $C^3\Pi_1-X^3\Delta_2$ subband, with comparatively narrow hyperfine widths. Three branches (R , Q , and P) are observed; Fig. 10 shows part of the Q branch of the (0,0) vibrational band at Doppler-limited resolution. The R lines are comparatively clear, as are the Q lines beyond $J \sim 12$, but the P lines are very badly blended by overlapping bands from various charge-transfer electronic transitions. Eventually the P lines were assigned by matching the observed line frequencies with those calculated from the positions of the R and Q lines. Small Λ doublings are observed in the high- J R lines with $J' \geq 35$. The rotational assignments and the electronic assignment of the lower state were based on the lower state combination differences, which were found to be the same as those of the $C^3\Pi_1-X^3\Delta_2$ (0,0) subband to within experimental error. The assignment of the upper state is not obvious from the laser excitation spectra since the R lines appear to be slightly stronger than the P lines, but the observation of a $^1\Pi-^1\Sigma^+$ emission transition following selective excitation to the upper state (see Sec. IX) secures its assignment.

It can be seen in Fig. 10 that the hyperfine widths of the rotational lines of the $e^1\Pi-X^3\Delta_2$ band are largest at low J and decrease as $1/J$; consequently the hyperfine structures of the very low J lines should contain the most hyperfine information. Unfortunately, under our experi-

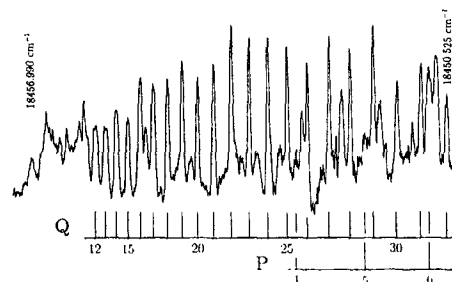


FIG. 10. The Q head of the $e^1\Pi-X^3\Delta_2$ (0,0) subband of NbN at Doppler-limited resolution.

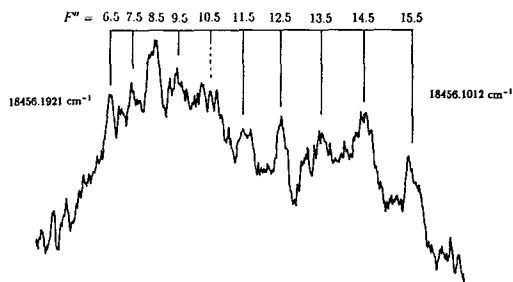


FIG. 11. Hyperfine structure of the $Q(11)$ line of the very weak $e^1\Pi-X^3\Delta_2(0,0)$ intercombination transition of NbN. This spectrum is a coadd of two 45 min scans taken under identical conditions, with a time constant of 10 s.

mental conditions, the low- J structure of this intercombination band is just not strong enough to be measurable at sub-Doppler resolution. As a compromise we recorded the sub-Doppler spectrum of the slightly stronger and unblended $Q(11)$ line. In order to obtain an acceptable signal-to-noise ratio, we recorded two spectra under identical scan conditions with a lock-in amplifier time constant of 10 s, and coadded them to give a single spectrum. The result is shown in Fig. 11.

The ten hyperfine lines observed in the spectrum are assigned as the ten $\Delta F = \Delta J$ hyperfine transitions. No $\Delta F \neq \Delta J$ lines are recognizable, so that the hyperfine splitting in the $J=11$ level of the $^1\Pi$ state cannot be measured directly. However, good values for the hyperfine energies of the $J=11$ level of the $^3\Delta_2$ state are available from the analysis of the $B^3\Phi-X^3\Delta$ system,⁴ and these allow the upper state hyperfine energies to be calculated from the line frequencies. The measured $Q(11)$ hyperfine line frequencies and the calculated upper state hyperfine energies are given in Table II; the assigned rotational lines of the $e^1\Pi-X^3\Delta_2(0,0)$ band are given in the Ph.D. thesis of G.H. Because of the strong perturbation between the e and C electronic states, a simultaneous data reduction of the two (0,0) vibrational bands has been attempted; this has permitted a detailed investigation of the spin and hyperfine structure of the $\delta\pi e^1\Pi/C^3\Pi$ complex.

TABLE II. Observed hyperfine transitions in the $e^1\Pi-X^3\Delta_2(0,0)$ $Q(11)$ line and calculated energies of the $^1\Pi, J=11$ hyperfine levels (in cm^{-1}).

$Q(11)$		$e^1\Pi, J=11$	
$F'-F''$	Frequency	F	Energy
15.5–15.5	18 456.1013	15.5	18 923.9879
14.5–14.5	18 456.1159	14.5	18 923.9936
13.5–13.5	18 456.1282	13.5	18 923.9975
12.5–12.5	18 456.1401	12.5	18 924.0014
11.5–11.5	18 456.1514	11.5	18 924.0051
10.5–10.5	18 456.1617	10.5	18 924.0084
9.5–9.5	18 456.1711	9.5	18 924.0113
8.5–8.5	18 456.1791	8.5	18 924.0134
7.5–7.5	18 456.1854	7.5	18 924.0143
6.5–6.5	18 456.1921	6.5	18 924.0162

VI. DETERMINATION OF MOLECULAR CONSTANTS FOR THE $e^1\Pi/C^3\Pi$ COMPLEX

Given the good accuracy of the molecular parameters of the $X^3\Delta$ state from the analysis of the intense $B^3\Phi-X^3\Delta$ system,⁴ we made no attempt to refine the lower state constants in the present analysis of the $e/C-X$ system. Our procedure has been to fit the complete sub-Doppler data set of the $C-X(0,0)$ transition, and the sub-Doppler and Doppler-limited data of the $e^1\Pi-X^3\Delta(0,0)$ transition, to the differences between the eigenvalues of the e/C Hamiltonian matrix and the energies of the $X^3\Delta, v=0$ state calculated from the constants of Ref. 4.

A. Rotational and hyperfine Hamiltonian

The rotational and hyperfine Hamiltonian for the $^1\Pi/3\Pi$ complex can be written as

$$\hat{H} = \hat{H}_{\text{rot}} + \hat{H}_{\text{so}} + \hat{H}_{\text{ss}} + \hat{H}_{\text{sr}} + \hat{H}_{\text{el,CD}} + \hat{H}_{\text{LD}} + \hat{H}_{\text{mag.hfs}} + \hat{H}_Q, \quad (4)$$

where the terms, written using operators appropriate for a case (a_β) basis, are

$$\begin{aligned} \hat{H}_{\text{rot}} = & B(\hat{J}^2 - \hat{J}_z^2 + \hat{S}^2 - \hat{S}_z^2 - \hat{J}_+ \hat{S}_- - \hat{J}_- \hat{S}_+) \\ & - D(\hat{J}^2 - \hat{J}_z^2 + \hat{S}^2 - \hat{S}_z^2 - \hat{J}_+ \hat{S}_- - \hat{J}_- \hat{S}_+)^2, \end{aligned} \quad (5)$$

$$\hat{H}_{\text{so}} = \sum_i a_i \hat{\mathbf{l}}_i \cdot \hat{\mathbf{s}}_i, \quad (6)$$

$$\hat{H}_{\text{ss}} = \frac{2}{3} \lambda (3\hat{S}_z^2 - \hat{S}^2), \quad (7)$$

$$\hat{H}_{\text{sr}} = \gamma (\hat{S}_z^2 - \hat{S}^2) + \frac{1}{2} \gamma (\hat{J}_+ \hat{S}_- + \hat{J}_- \hat{S}_+), \quad (8)$$

$$\begin{aligned} \hat{H}_{\text{el,CD}} = & \frac{1}{2} A_D \left[\sum_i \hat{\mathbf{l}}_i \cdot \hat{\mathbf{s}}_i, \hat{J}^2 - \hat{J}_z^2 + \hat{S}^2 - \hat{S}_z^2 - \hat{J}_+ \hat{S}_- - \hat{J}_- \hat{S}_+ \right]_+ \\ & + \frac{1}{3} \lambda_D [3\hat{S}_z^2 - \hat{S}^2, \hat{J}^2 - \hat{J}_z^2 + \hat{S}^2 - \hat{S}_z^2 - \hat{J}_+ \hat{S}_- \\ & - \hat{J}_- \hat{S}_+]_+ \end{aligned} \quad (9)$$

$$\begin{aligned} \hat{H}_{\text{LD}} = & \frac{1}{2} (o + p + q) (\hat{S}_+^2 + \hat{S}_-^2) \\ & - \frac{1}{2} (p + 2q) (\hat{J}_+ \hat{S}_+ + \hat{J}_- \hat{S}_-) + \frac{1}{2} q (\hat{J}_+^2 + \hat{J}_-^2), \end{aligned} \quad (10)$$

$$\begin{aligned} \hat{H}_{\text{mag.hfs}} = & a \hat{\mathbf{l}}_z \hat{L}_z + \sum_i b_{Fi} \hat{\mathbf{l}}_i \cdot \hat{\mathbf{s}}_i - \sum_i g \mu_B g_N \mu_N r^{-3} \sqrt{10} T^1(\hat{\mathbf{l}}) \\ & \cdot T^1(\hat{\mathbf{s}}_i, \hat{C}_i^{(2)}), \end{aligned} \quad (11)$$

$$\hat{H}_Q = e^2 Q q_0 \frac{3\hat{I}_z^2 - \hat{I}^2}{4I(2I-1)}. \quad (12)$$

The terms in Eq. (4) can be identified by their subscripts. \hat{H}_{rot} is the rotational Hamiltonian; \hat{H}_{so} , \hat{H}_{ss} , and \hat{H}_{sr} are, respectively, the electron spin-orbit, spin-spin, and spin-rotation interactions, while $\hat{H}_{\text{el,CD}}$ represents the centrifugal distortion corrections to \hat{H}_{so} and \hat{H}_{ss} ; \hat{H}_{LD} is the

TABLE III. The structure of the ${}^1\Pi/{}^3\Pi$ matrix in a Hund's case (a) parity basis.^a

		$ J\rangle$			
		$ {}^1\Pi(\frac{d}{s}\frac{f}{e})\rangle$	$ {}^3\Pi_2(\frac{s}{d}\frac{f}{e})\rangle$	$ {}^3\Pi_1(\frac{s}{d}\frac{f}{e})\rangle$	$ {}^3\Pi_0(\frac{s}{d}\frac{f}{e})\rangle$
$\langle J $	$\langle {}^1\Pi(\frac{d}{s}\frac{f}{e}) $	$\mathcal{A}^{(1)} \mp \mathcal{F}^{(1)}$	$-\beta$	α	β
	$\langle {}^3\Pi_2(\frac{s}{d}\frac{f}{e}) $	$-\beta$	\mathcal{A}	\mathcal{B}	$\pm \mathcal{F}_{20}$
	$\langle {}^3\Pi_1(\frac{s}{d}\frac{f}{e}) $	α	\mathcal{B}	$\mathcal{A} \pm \mathcal{F}_{1,-1}$	$\mathcal{B} \mp \mathcal{K}_{10}$
	$\langle {}^3\Pi_0(\frac{s}{d}\frac{f}{e}) $	β	$\pm \mathcal{F}_{20}$	$\mathcal{B} \mp \mathcal{K}_{10}$	$\mathcal{A} \pm \mathcal{C}$
$\langle J-1 $	$\langle {}^1\Pi(\frac{s}{d}\frac{e}{f}) $	$-\mathcal{C}^{(1)} \pm \mathcal{G}^{(1)}$	$-\delta_{12}$	$-\gamma$	$-\delta_{10}$
	$\langle {}^3\Pi_2(\frac{d}{s}\frac{e}{f}) $	δ_{21}	$-\mathcal{C}_2$	$-\mathcal{D}_{21}$	$\mp \mathcal{G}_{20}$
	$\langle {}^3\Pi_1(\frac{d}{s}\frac{e}{f}) $	$-\gamma$	\mathcal{D}_{12}	$-\mathcal{C}_1 \mp \mathcal{G}_{11}$	$-\mathcal{D}_{10} \pm \mathcal{L}_{10}$
	$\langle {}^3\Pi_0(\frac{d}{s}\frac{e}{f}) $	δ_{01}	$\mp \mathcal{G}_{02}$	$\mathcal{D}_{01} \pm \mathcal{L}_{01}$	$-\mathcal{C}_0$
$\langle J-2 $	$\langle {}^1\Pi(\frac{d}{s}\frac{f}{e}) $	$\mathcal{G}^{(1)} + \mathcal{K}^{(1)}$			
	$\langle {}^3\Pi_2(\frac{s}{d}\frac{f}{e}) $		\mathcal{E}_2		$\pm \mathcal{H}_{20}$
	$\langle {}^3\Pi_1(\frac{s}{d}\frac{f}{e}) $			$\mathcal{E}_1 \pm \mathcal{K}_{11}$	
	$\langle {}^3\Pi_0(\frac{s}{d}\frac{f}{e}) $		$\pm \mathcal{K}_{02}$		\mathcal{E}_0

^aThe superscript (1) refers to the ${}^1\Pi$ state; subscripts are used, where necessary, to indicate the Ω values of the combining basis functions. The upper and lower signs give the (e or f) parity labels; the symbols s and d indicate the Wang sum and difference functions, respectively [see Eq. (17)].

Λ -doubling operator, and finally $\hat{H}_{\text{mag,hfs}}$ and \hat{H}_Q are the nuclear magnetic and electric quadrupole hyperfine Hamiltonian operators, respectively. The symbol $[x,y]_+ = xy + yx$ is the anticommutator, which is required to preserve the Hermitian form of the matrices.¹³ The parameter a_i in Eq. (6) is the spin-orbit interaction constant of electron i , not to be confused with the coefficient of the $\mathbf{I} \cdot \mathbf{L}$ term in the nuclear magnetic hyperfine Hamiltonian. In Eq. (11), the second term is the Fermi contact interaction, while the third term includes the dipolar interaction represented by the parameter c ,¹⁴

$$c = 3g\mu_B g_N \mu_N \langle \Lambda | r^{-3} T_0^2(C) | \Lambda \rangle, \quad (13)$$

and the hyperfine Λ -doubling term represented by the coefficient d :

$$d = -\sqrt{6}g\mu_B g_N \mu_N \langle \Lambda \pm 1 | r^{-3} T_{\pm 2}^2(C) | \Lambda \mp 1 \rangle. \quad (14)$$

The interactions between the ${}^1\Pi$ and ${}^3\Pi$ states are caused by the matrix elements of the spin-orbit and magnetic hyperfine Hamiltonians off-diagonal in S ; the explicit forms for the matrix elements diagonal in J are

$$\langle \pm \Lambda; S=1, \Sigma=0; J\Omega IF | \hat{H}_{\text{so}} + \hat{H}_{\text{mag,hfs}} | \pm \Lambda;$$

$$S=0, \Sigma=0; J\Omega IF \rangle$$

$$= \pm \mathcal{A}^{(2)} \pm \frac{\Omega[b^{(2)} + c^{(2)}]}{2J(J+1)} [F(F+1) - I(I+1) - J(J+1)]. \quad (15)$$

For comparison, the elements diagonal in S and J are¹⁵

$$\begin{aligned} &\langle \pm \Lambda; S\Sigma; J\Omega IF | \hat{H}_{\text{so}} + \hat{H}_{\text{mag,hfs}} | \pm \Lambda; S\Sigma; J\Omega IF \rangle \\ &= A\Lambda\Sigma + \frac{\Omega[a\Lambda + (b+c)\Sigma]}{2J(J+1)} [F(F+1) - I(I+1) - J(J+1)]. \end{aligned} \quad (16)$$

In these equations the diagonal spin-orbit and hyperfine parameters, A , b , and c are not to be confused with the off-diagonal parameters $\mathcal{A}^{(2)}$, $b^{(2)}$, and $c^{(2)}$. In the single configuration approximation, where the ${}^1\Pi/{}^3\Pi$ complex is described by the configuration $\delta\pi$, the various interaction parameters are related to the one-electron parameters for the δ and π electrons by

$$A\Lambda = a_\delta - \frac{1}{2}a_\pi, \quad A^{(2)} = a_\delta + \frac{1}{2}a_\pi,$$

$$b = \frac{1}{2}(b_\delta + b_\pi), \quad b^{(2)} = \frac{1}{2}(b_\delta - b_\pi),$$

$$c = \frac{1}{2}(c_\delta + c_\pi), \quad c^{(2)} = \frac{1}{2}(c_\delta - c_\pi),$$

where x_δ and x_π are the coupling constants for the δ and π electrons, respectively.

It can be shown by second-order perturbation theory that the spin-orbit interaction between the $^1\Pi$ and $^3\Pi$ states, represented by the constant $A^{(2)}$, produces correction terms to the $^3\Pi$ state that have the same forms as the electron spin-spin and spin-rotation interaction terms. In other words, the spin parameters λ and γ are highly correlated to the parameter $A^{(2)}$, and cannot be determined separately. We have therefore omitted the λ and γ terms in our full matrix treatment of the $^1\Pi/{}^3\Pi$ complex, retaining only the off-diagonal spin-orbit parameter, $A^{(2)}$, and its centrifugal distortion correction term, $A_D^{(2)}$. The structure of the Hamiltonian matrix that we have used for the $\delta\pi$ $^1\Pi/{}^3\Pi$ complex of NbN is given as Table III, with the nonzero matrix elements indicated by various symbols; the exact meanings of these symbols are given in Table IV.

The Hamiltonian matrix for the interacting $^1\Pi$ and $^3\Pi$ states has eight basis functions for each J in the general case, since Λ takes the values ± 1 . The 8×8 matrix can be factorized into two 4×4 matrices by transforming to the Hund's case (a) parity basis

$$|J\pm\rangle = \frac{1}{\sqrt{2}} (|\Lambda; S\S\S; J\Omega\rangle \pm |-\Lambda; S-\Sigma\S; J-\Omega\rangle). \quad (17)$$

In this equation, the sum and difference functions (written s and d in Table III) correspond, respectively, to the e and f parity labels in the $^1\Pi$ state, and to the f and e parities in the $^3\Pi$ state. The e, f parity labels of the basis functions must of course alternate with J , as can be seen in Table III.

B. Least-squares results

The final set of parameters for the $^1\Pi/{}^3\Pi$, $v=0$ complex, determined by an iterative least-squares fit, is given in Table V. The 1400 data points consisted mostly of the hyperfine transitions from the three $^3\Pi-{}^3\Delta$ (0,0) subbands, accurately calibrated to within 10 MHz, and some data from the $^1\Pi-{}^3\Delta_2$ (0,0) transition, including the ten $Q(11)$ hyperfine lines and the less accurate Doppler-limited rotational lines (which were given a weight of 0.05). The standard deviation of the fit was 0.0005 cm^{-1} (15 MHz), which is comparable to the uncertainty of the spectral data. The line frequencies are listed in the M.Sc. and Ph.D. theses of G.H.

It is clear from our data that the Fermi contact parameter b of the $C^3\Pi$ state is effectively zero, since the standard deviation increases marginally when b is floated. The off-diagonal Fermi contact parameter $b^{(2)}$ between the singlet and triplet Π states is well determined, but has the surprisingly large value, $b^{(2)} = -0.0949 \text{ cm}^{-1}$. It is not certain if this is real or whether it is an artifact of the approximations used (see Sec. VIII).

TABLE IV. Matrix element representations of the labels used in Table III.^a

$\mathcal{A} = \langle \Lambda; S\S\S; J\Omega IF \hat{H}_{\text{rot}} + \hat{H}_{\text{so}} + \hat{H}_{\text{ss}} + \hat{H}_{\text{sr}} + \hat{H}_{\text{el,CD}} + \hat{H}_{\text{mag,hfs}} + \hat{H}_Q \Lambda; S\S\S; J\Omega IF \rangle$
$\mathcal{B} = \langle \Lambda; S\S\S \pm 1; J\Omega \pm 1 IF \hat{H}_{\text{rot}} + \hat{H}_{\text{sr}} + \hat{H}_{\text{el,CD}} + \hat{H}_{\text{mag,hfs}} \Lambda; S\S\S; J\Omega IF \rangle$
$-\mathcal{C} = \langle \Lambda; S\S\S; J-1\Omega 1 IF \hat{H}_{\text{mag,hfs}} + \hat{H}_Q \Lambda; S\S\S; J\Omega IF \rangle$
$\mp \mathcal{D} = \langle \Lambda; S\S\S \pm 1; J-1\Omega \pm 1 IF \hat{H}_{\text{mag,hfs}} \Lambda; S\S\S; J\Omega IF \rangle$
$\mathcal{E} = \langle \Lambda; S\S\S; J-2\Omega IF \hat{H}_Q \Lambda; S\S\S; J\Omega IF \rangle$
$\mathcal{F} = \langle \Lambda \pm 2; S\S\S; J\Omega \pm 2 IF \hat{H}_{\text{LD}} + \hat{H}_Q \Lambda; S\S\S; J\Omega IF \rangle$
$\mp \mathcal{G} = \langle \Lambda \pm 2; S\S\S; J-1\Omega \pm 2 IF \hat{H}_Q \Lambda; S\S\S; J\Omega IF \rangle$
$\mathcal{H} = \langle \Lambda \pm 2; S\S\S; J-2\Omega \pm 2 IF \hat{H}_Q \Lambda; S\S\S; J\Omega IF \rangle$
$-\mathcal{K} = \langle \Lambda \pm 2; S\S\S \mp 1; J\Omega \pm 1 IF \hat{H}_{\text{LD}} \Lambda; S\S\S; J\Omega IF \rangle$
$\pm \mathcal{L} = \langle \Lambda \pm 2; S\S\S \mp 1; J-1\Omega \pm 1 IF \hat{H}_{\text{mag,hfs}} \Lambda; S\S\S; J\Omega IF \rangle$
$\pm \mathcal{O} = \langle \Lambda \pm 2; S\S\S \mp 2; J\Omega IF \hat{H}_{\text{LD}} \Lambda; S\S\S; J\Omega IF \rangle$
$\alpha = \langle ^1\Pi, \Lambda = \pm 1; J\Omega IF \hat{H}_{\text{so}} + \hat{H}_{\text{mag,hfs}} ^3\Pi, \Lambda = \pm 1; J\Omega IF \rangle$
$= \Lambda A^{(2)} + \Lambda [b^{(2)} + c^{(2)}] \frac{\Omega W(FIJ)}{2J(J+1)}$
$\pm \beta = \langle ^1\Pi; J\Omega IF \hat{H}_{\text{mag,hfs}} ^3\Pi; J\Omega \pm 1 IF \rangle$
$= \pm b^{(2)} \frac{W(FIJ) \sqrt{J(J+1) - \Omega(\Omega \pm 1)}}{2\sqrt{2}J(J+1)}$
$-\gamma = \langle ^1\Pi; J-1\Omega IF \hat{H}_{\text{mag,hfs}} ^3\Pi_1; J\Omega IF \rangle$
$= -[b^{(2)} + c^{(2)}] \frac{Y(FIJ)}{2J} \sqrt{\frac{J^2-1}{4J^2-1}}$
$+\delta = \langle ^1\Pi; J\Omega IF \hat{H}_{\text{mag,hfs}} ^3\Pi; J-1\Omega \pm 1 IF \rangle$
$= +b^{(2)} \frac{Y(FIJ)}{2J} \sqrt{\frac{(J+1-\Omega \mp 1)(J-\Omega \mp 1)}{2(2J-1)(2J+1)}}$
$-\delta = \langle ^1\Pi; J-1\Omega IF \hat{H}_{\text{mag,hfs}} ^3\Pi; J\Omega \pm 1 IF \rangle$
$= -b^{(2)} \frac{Y(FIJ)}{2J} \sqrt{\frac{(J-1+\Omega \pm 1)(J+\Omega \pm 1)}{2(2J-1)(2J+1)}}$

^a $W(FIJ) = F(F+1) - I(I+1) - J(J+1)$; $Y(FIJ) = [(F+I+J+1)(I+J-F)(F+J-I)(F+I-J+1)]^{1/2}$. Matrix elements diagonal in S are labeled by upper case script letters; algebraic expressions have been given by Ref. 15. Matrix elements between the $^1\Pi$ and $^3\Pi$ states are labeled by lower case Greek letters. The signs in front of the letters are those of the matrix elements.

VII. HYPERFINE ANALYSIS OF THE $f^1\Phi-a^1\Delta$ SYSTEM

A. Spectral characteristics

An emission band at $17\,115 \text{ cm}^{-1}$, first observed by Dunn,¹⁶ was originally thought to arise from a $^1\Pi-{}^1\Sigma^+$ electronic transition. However dispersed fluorescence studies (see Sec. IX C) have shown that the lower state is the $^1\Delta$, $v=0$ level, and that the relative branch intensities are consistent with $\Delta\Lambda = +1$ selection rules, proving that it is a $^1\Phi-{}^1\Delta$ transition. The $^1\Phi$ upper state, here designated $f^1\Phi$, comes from the same electron configuration, $\delta\pi$, as the $B^3\Phi$ state. The $a^1\Delta$ lower state lies at 5197 cm^{-1} and, like the $X^3\Delta$ state, comes from the configuration $\sigma\delta$. As

TABLE V. Deperturbed rotational and hyperfine constants for the $e^1\Pi$ and $C^3\Pi$ states together with the interaction parameters. Values in cm^{-1} .^a

Parameter	$^3\Pi$		$^1\Pi$	
T	17 674.369 4	± 1	17 776.949 3	± 10
B	0.496 257 9	± 4	0.494 886	± 9
$10^6 D$	0.490 5	± 3	0.517	± 6
A	201.471 1	± 1		
$10^4 A_D$	0.213	± 3		
a	0.011 3	± 10	0.006 4	± 21
b	0.0	fixed		
c	0.005 8	± 10		
d	-0.003 0	± 10		
$e^2 Q q_0$	0.002 5	± 6		
$o+p+q$	3.305 3	± 1		
$p+2q$	0.062 5	± 5		
q	-0.001 35	± 13	0.001 0	± 12

Interaction parameters			
$A^{(2)}$	697.8873	± 3	
$10^3 A_D^{(2)}$	-0.535	± 12	
$b^{(2)}$	-0.0949	± 8	
$c^{(2)}$	0.0126	± 19	

^aThe energy zero for T is the spin-free energy of $X^3\Delta$, 432.04₀₇ cm^{-1} above $X^3\Delta_1$. Errors quoted are three standard deviations, in units of the last significant figure given. $\sigma=0.000\ 50\ \text{cm}^{-1}$.

explained in Sec. II, the $f^1\Phi-a^1\Delta$ transition could only be observed by laser excitation if the discharge was run at low pressure, so as to minimize the collisional quenching of the metastable $a^1\Delta$ lower state; under these conditions it was intense enough for sub-Doppler work.

The hyperfine structure of the $f^1\Phi-a^1\Delta$ transition is particularly interesting because it means that there is now information available for *all* the electronic states from the configurations $\sigma\delta$ and $\delta\pi$. It becomes possible to make detailed comparisons of the hyperfine parameters, and to fill in the details of the second-order spin-orbit/Fermi contact perturbation between the $a^1\Delta$ and $X^3\Delta$ states described in Ref. 4. A similar, though rather smaller, spin-orbit/Fermi contact perturbation is found to occur between the $f^1\Phi$ and $B^3\Phi$ states.

The $^1\Phi-^1\Delta$ (0,0) band lies between the $^3\Phi_2-^3\Delta_1$ (1,0) subband at 17 131 cm^{-1} and the (2,1) subband at 17 075 cm^{-1} ; it is very simple in appearance, with single R , Q , and P branches, and no Λ doubling. The hyperfine widths of the rotational lines are moderate at low J and decrease as $1/J$. Figures 12 and 13 show, respectively, the hyperfine structures of the Q branch head and the $R(3)$ line at sub-Doppler resolution. The resolved hyperfine structure can mostly be assigned as the $\Delta F=\Delta J$ hyperfine components; these are usually the strongest components of a rotational line, and show the characteristic Landé-type pattern. Some weak $\Delta F\neq\Delta J$ hyperfine satellites are also observed in the first two R and Q lines. These hyperfine satellites are invariably grouped with the hyperfine main lines with the same value of F' , which indicates that the hyperfine splittings of the lower state are much smaller than those of the

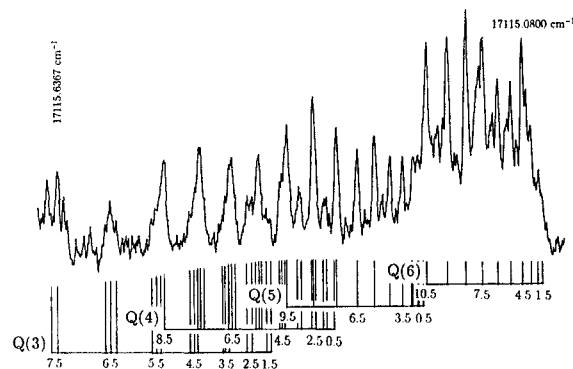


FIG. 12. Hyperfine line assignments in the Q head of the $f^1\Phi-a^1\Delta$ (0,0) band of NbN.

upper state. The relative intensities of the $\Delta F=\Delta J$ main lines and the hyperfine satellites change dramatically with F at very low J . This was an important consideration in making the hyperfine assignments; for instance, in the $Q(3)$ line of Fig. 12, the hyperfine main lines are fairly strong in the $F'=7\frac{1}{2}$, $6\frac{1}{2}$, and $5\frac{1}{2}$ groups, while the hyperfine satellites are almost unrecognizable, but in the $F'=4\frac{1}{2}$ and $3\frac{1}{2}$ groups, the hyperfine main lines become very weak and, in the $F'=2\frac{1}{2}$ group, the main line disappears and the two lines observed are the $F'-F''=2\frac{1}{2}-1\frac{1}{2}$ and $2\frac{1}{2}-3\frac{1}{2}$ satellite lines. The disappearance of the $2\frac{1}{2}-2\frac{1}{2}$ component is caused by an intensity cancellation of the type reported in various Q lines of the NbO spectrum;¹⁷ it occurs when the vectors \mathbf{J} and \mathbf{F} would be at right angles in a classical model.

B. Determination of molecular constants for the $a^1\Delta$ and $f^1\Phi$ states

For a singlet electronic state, where the spin angular momentum \mathbf{S} is zero, the effective Hamiltonian consists only of the rotational part, the $\mathbf{I}\cdot\mathbf{L}$ hyperfine term and a quadrupole term which we shall ignore. Therefore \hat{H} can be written

$$\hat{H} = B\hat{\mathbf{R}}^2 - D\hat{\mathbf{R}}^4 + a\hat{\mathbf{I}}\cdot\hat{\mathbf{L}}, \quad (18)$$

where $\mathbf{R}=\mathbf{J}-\mathbf{L}-\mathbf{S}$ is the rotational angular momentum, \mathbf{I} is the nuclear spin angular momentum, and \mathbf{L} the electron orbital angular momentum. The Hamiltonian matrix for a singlet state is simple, consisting of diagonal elements given by¹⁵

$$\begin{aligned} \langle JIF\Omega | \hat{H}_{\text{rot}} + \hat{H}_{\text{mag,hfs}} | JIF\Omega \rangle \\ = T_0 + BJ(J+1) - DJ^2(J+1)^2 \\ + a\Lambda \frac{\Omega[F(F+1) - I(I+1) - J(J+1)]}{2J(J+1)}, \end{aligned} \quad (19)$$

and $\Delta J=\pm 1$ off-diagonal hyperfine elements, given by

$$\langle J-1, IF\Omega | \hat{H}_{\text{rot}} + \hat{H}_{\text{mag.hfs}} | JIF\Omega \rangle = -a\Lambda \frac{\sqrt{J^2 - \Omega^2} \sqrt{(I+J+F+1)(J+I-F)(F+J-I)(F+I-J+1)}}{2J\sqrt{4J^2 - 1}}. \quad (20)$$

For each value of the F quantum number there are either $(2I+1)$ or $(2F+1)$ basis functions, representing the possible $|J\rangle$ functions for each F , and the Hamiltonian matrix is either a $(2I+1) \times (2I+1)$ or $(2F+1) \times (2F+1)$ matrix, whichever is smaller. A simple nonlinear least-squares fitting program was accordingly written to fit the measured hyperfine line frequencies of the $f^1\Phi - a^1\Delta$ (0,0) transition to the differences of eigenvalues of the upper and lower state matrices. The derived rotational and hyperfine constants for the $^1\Phi$ and $^1\Delta$ states are given in Table VI, while the spectral lines used in the fit are listed in the Ph.D. thesis of G.H.

The B constant for the $a^1\Delta$ state is slightly larger than that of the $X^3\Delta$ ground state; this is similar to what is found in TiO and VO, where the lower spin-multiplicity states arising from the same electron configurations as the ground states have slightly larger B constants.^{18,19}

VIII. DISCUSSION OF THE SPIN AND HYPERFINE STRUCTURE IN THE ELECTRON CONFIGURATIONS $\sigma\delta$ AND $\delta\pi$

Since, with this work, rotational and hyperfine constants are now available for all six electronic states from the configurations $\sigma\delta$ and $\delta\pi$, some interesting comparisons can be made. The values are given in Table VII. In the following discussion we show that the spin-orbit and hyperfine parameters can be interpreted very satisfactorily in terms of the single configuration approximation, after correcting for the interactions between the states of a given configuration.

A. The spin-orbit coupling

The spin-orbit effects, both within a single electronic state and between two electronic states, can be written in terms of spin-orbit coupling parameters for the individual electrons. In the single configuration approximation, the following matrix elements are expected for the electronic states from the configurations $\sigma\delta$ and $\delta\pi$:

$$\langle \sigma\delta^3\Delta_3 | \hat{H}_{\text{so}} | \sigma\delta^3\Delta_3 \rangle = -\langle \sigma\delta^3\Delta_1 | \hat{H}_{\text{so}} | \sigma\delta^3\Delta_1 \rangle = a_\delta, \quad (21)$$

$$\langle \sigma\delta^1\Delta_2 | \hat{H}_{\text{so}} | \sigma\delta^3\Delta_2 \rangle = a_\delta, \quad (22)$$

$$\begin{aligned} \langle \delta\pi^3\Phi_4 | \hat{H}_{\text{so}} | \delta\pi^3\Phi_4 \rangle &= -\langle \delta\pi^3\Phi_2 | \hat{H}_{\text{so}} | \delta\pi^3\Phi_2 \rangle \\ &= a_\delta + \frac{1}{2}a_\pi, \end{aligned} \quad (23)$$

$$\langle \delta\pi^1\Phi_3 | \hat{H}_{\text{so}} | \delta\pi^3\Phi_3 \rangle = a_\delta - \frac{1}{2}a_\pi, \quad (24)$$

$$\begin{aligned} \langle \delta\pi^3\Pi_2 | \hat{H}_{\text{so}} | \delta\pi^3\Pi_2 \rangle &= -\langle \delta\pi^3\Pi_0 | \hat{H}_{\text{so}} | \delta\pi^3\Pi_0 \rangle \\ &= a_\delta - \frac{1}{2}a_\pi, \end{aligned} \quad (25)$$

$$\langle \delta\pi^1\Pi_1 | \hat{H}_{\text{so}} | \delta\pi^3\Pi_1 \rangle = a_\delta + \frac{1}{2}a_\pi. \quad (26)$$

In these equations, a_δ and a_π are the spin-orbit coupling constants for the δ and π electrons, respectively. Experimental numbers are available for the diagonal spin-orbit couplings, $A\Lambda$, in the $^3\Delta$, $^3\Phi$, and $^3\Pi$ states; also the off-diagonal spin-orbit coupling between the $^1\Pi$ and $^3\Pi$ states has been obtained as

$$\langle ^1\Pi_1 | \hat{H}_{\text{so}} | ^3\Pi_1 \rangle = 697.9 \text{ cm}^{-1} \quad (27)$$

(see Table V). Although no direct measurements of the off-diagonal couplings between $^1\Delta$ and $^3\Delta$, or between $^1\Phi$ and $^3\Phi$, have been made, they can be calculated from the observed positions of the interacting states by “undiaagonalizing” the 2×2 interaction matrices^{4,20} for the $\Sigma=0$ components, assuming that no other interactions are occurring. From the energies of the $^1\Delta$, $^3\Delta$, $^1\Phi$, and $^3\Phi$ states given in Fig. 1, we find

$$\langle ^1\Delta_2 | \hat{H}_{\text{so}} | ^3\Delta_2 \rangle = 462.4 \text{ cm}^{-1}, \quad (28)$$

$$\langle ^1\Phi_3 | \hat{H}_{\text{so}} | ^3\Phi_3 \rangle = 154.9 \text{ cm}^{-1}. \quad (29)$$

Now a simple comparison of the magnitudes of the diagonal and off-diagonal spin-orbit couplings should give a measure of how well the single configuration approximation holds. According to Eqs. (21)–(26), the off-diagonal couplings, $\langle ^1\Delta | \hat{H}_{\text{so}} | ^3\Delta \rangle$, $\langle ^1\Phi | \hat{H}_{\text{so}} | ^3\Phi \rangle$, and $\langle ^1\Pi | \hat{H}_{\text{so}} | ^3\Pi \rangle$

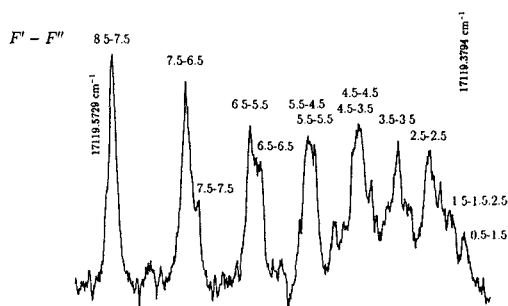


FIG. 13. Hyperfine structure of the $R(3)$ line of the $f^1\Phi - a^1\Delta$ (0,0) band of NbN. The $a^1\Delta$ lower state lies 5197 cm^{-1} above $X^3\Delta_1$.

TABLE VI. Molecular constants of the $f^1\Phi$ and $a^1\Delta$ states of NbN (values in cm^{-1}).^a

Parameter	$^1\Delta$	$^1\Phi$
$T(\nu=0)$	0.0 ^b	17 115.683 8 ^c
B	0.508 27 ± 4	0.495 09 ± 5
$10^6 D$	0.420 ± 147	0.490 ± 149
$a\Lambda$	0.005 4 ± 3	0.036 9 ± 2
Standard deviation = 0.000 42		

^aError limits are three standard deviations in units of the last significant figure quoted.

^bThe absolute energy position of $a^1\Delta$, $\nu=0$ is 5197.2 cm^{-1} , determined from the origin of the $C^3\Pi_1 - a^1\Delta(0,0)$ transition (Sec. IX A).

^cThe absolute rotationless energy of $f^1\Phi$, $\nu=0$ is $22\,312.9 \text{ cm}^{-1}$.

TABLE VII. Comparisons of the molecular constants for the electronic states from the configurations $\sigma\delta$ and $\delta\pi$ of NbN^a (values in cm⁻¹).

States	T_0	B_0	$r_0/\text{\AA}$	$A\Lambda$	$a\Lambda$	$(b+c)$
$f^1\Phi$	21 880.9	0.495 09	1.672 6		0.036 9	
$e^1\Pi$	17 776.949	0.494 886	1.672 92		0.006 4	
$C^3\Pi$	17 674.3694	0.496 257 9	1.670 608	201.47	0.011 3	~ 0
$B^3\Phi$	16 518.5565	0.495 813 4	1.671 357	807.39	0.040 07	-0.023 22
$a^1\Delta$	4 765.2	0.508 27	1.650 8		0.005 4	
$X^3\Delta$	0	0.501 464 1	1.661 913	448.56	0.024 85	0.086 42

^aConstants for the $X^3\Delta$ and $B^3\Phi$ states are taken from Ref. 4. The $a\Lambda$ values have been corrected for spin-orbit/Fermi contact distortion, except for the $f^1\Phi$ and $a^1\Delta$ states. The T_0 's are given relative to the spin-free energy of the $X^3\Delta$ state as zero; the positions of the spin substates relative to the energy of the $X^3\Delta_1$ component as zero are given in Fig. 1.

should equal the diagonal elements in the $^3\Delta$, $^3\Pi$, and $^3\Phi$ states, respectively. The values are compared in Table VIII. The agreement is very good for the $^1\Delta$ and $^3\Delta$ states of the configuration $\sigma\delta$, but the diagonal elements are somewhat larger than the off diagonal for the configuration $\delta\pi$; converting these to one-electron parameters, it is seen that the various values agree to within 10%–15%. This is fairly typical for molecules such as NbN, and there can be no doubt about the electron configurations.

B. The hyperfine a parameters

Like the spin-orbit coupling constants, the hyperfine a parameters for degenerate electronic states are simply related to one-electron parameters in the single configuration approximation. In this section the symbol a is the coefficient of the $\mathbf{I} \cdot \mathbf{L}$ term in the magnetic hyperfine Hamiltonian, rather than a spin-orbit parameter.

It is easy to show that the hyperfine parameters a for the $X^3\Delta$, $B^3\Phi$, and $C^3\Pi$ states can be expressed in terms of one-electron hyperfine parameters as

$$a\Lambda(^3\Delta) = 2a_\delta; \quad a\Lambda(^3\Phi) = 2a_\delta + a_\pi; \quad (30)$$

$$a\Lambda(^3\Pi) = 2a_\delta - a_\pi,$$

from which it follows that

$$2a\Lambda(^3\Delta) - a\Lambda(^3\Phi) = a\Lambda(^3\Pi). \quad (31)$$

Substituting the $a\Lambda$ values of the $^3\Delta$ and $^3\Phi$ states given in Table VII, we find

$$2a\Lambda(^3\Delta) - a\Lambda(^3\Phi) = 0.009 63 \text{ cm}^{-1}, \quad (32)$$

which is to be compared to the $a\Lambda$ value for the $C^3\Pi$ state, 0.0113 cm⁻¹. The agreement is very reasonable, and is similar to what was found for the spin-orbit parameters. On the other hand Table VII shows that the $a\Lambda$ values for the $^1\Pi$ and $^3\Pi$ states are not as close as they should be, since a is not expected to depend on the electron spin state. The value of $a\Lambda(^3\Pi)$ seems to be correct because of the large amount of hyperfine data available, and the consistency of Eqs. (30)–(32). The reason for the discrepancy appears to be that the $a\Lambda$ value for the $^1\Pi$ state is less well determined, having been derived from a very limited amount of hyperfine data, and also using a “unique perturber” model²¹ for the deperturbation. There is no doubt

that a deperturbation is needed, though, for if the value of $a\Lambda(^1\Pi)$ is calculated directly from the hyperfine energies given in Table II, it is found to be -0.0361 cm⁻¹; this is in gross disagreement with the value $a\Lambda(^3\Pi) = 0.0113 \text{ cm}^{-1}$, even having the wrong sign. This wrong sign is in fact an extreme example of spin-orbit/Fermi contact distortion of the nuclear spin-electron orbit hyperfine interaction, which we now describe for the $a^1\Delta$ and $f^1\Phi$ states.

The $a\Lambda$ parameters for the $a^1\Delta$ and $f^1\Phi$ states given in Table VII have been derived from an effective Hamiltonian for singlet electronic states, and therefore cannot be compared directly to the $a\Lambda$ values for the $^3\Delta$ and $^3\Phi$ states. This is because the apparent $a\Lambda$ parameters contain the effects of the spin-orbit/Fermi contact cross term between the singlet and triplet states from the same electron configuration.⁴ The effect can be understood from the form of Eq. (15). If second-order perturbation theory is applied to Eq. (15) it produces a correction to the energy of the singlet state that can be expressed as

$$\Delta E = \frac{1}{E_{\text{singlet}}^0 - E_{\text{triplet}}^0} \left([A^{(2)}]^2 + \frac{2A^{(2)}[b^{(2)} + c^{(2)}]\Omega}{2J(J+1)} \times W(FIJ) + \frac{[b^{(2)} + c^{(2)}]^2 \Omega^2}{4J^2(J+1)^2} W^2(FIJ) \right), \quad (33)$$

where

$$W(FIJ) = [F(F+1) - I(I+1) - J(J+1)] \quad (34)$$

and $A^{(2)}$, $b^{(2)}$, and $c^{(2)}$ are the same second-order parameters as in Eq. (15). There are three terms in Eq. (33); the first term is the correction to the term value of the singlet

TABLE VIII. Comparisons of the first-order and second-order spin-orbit coupling matrix elements in the electron configurations $\sigma\delta$ and $\delta\pi$ of NbN.^a

$\langle \sigma\delta^3\Delta_3 \hat{H}_{so} \sigma\delta^3\Delta_3 \rangle = 448.56 \text{ cm}^{-1}$	$\langle \sigma\delta^1\Delta_2 \hat{H}_{so} \sigma\delta^3\Delta_2 \rangle = 462.4 \text{ cm}^{-1}$
$\langle \delta\pi^3\Phi_4 \hat{H}_{so} \delta\pi^3\Phi_4 \rangle = 807.39 \text{ cm}^{-1}$	$\langle \delta\pi^1\Pi_1 \hat{H}_{so} \delta\pi^3\Pi_1 \rangle = 697.9 \text{ cm}^{-1}$
$\langle \delta\pi^3\Pi_2 \hat{H}_{so} \delta\pi^3\Pi_2 \rangle = 201.47 \text{ cm}^{-1}$	$\langle \delta\pi^1\Phi_3 \hat{H}_{so} \delta\pi^3\Phi_3 \rangle = 154.9 \text{ cm}^{-1}$

^aDerived parameters: (1) From the diagonal spin-orbit couplings, $a_\delta = 448.56 \text{ cm}^{-1}$ in the configuration $\sigma\delta$ or 504.43 cm^{-1} in the configuration $\delta\pi$; $\frac{1}{2}a_\pi = 302.96 \text{ cm}^{-1}$ in the configuration $\delta\pi$. (2) From the off-diagonal matrix elements, $a_\delta = 462.4 \text{ cm}^{-1}$ in the configuration $\sigma\delta$ or 426.4 cm^{-1} in the configuration $\delta\pi$; $\frac{1}{2}a_\pi = 271.5 \text{ cm}^{-1}$ in the configuration $\delta\pi$.

state, while the second term has the same quantum number dependence as the diagonal hyperfine matrix element for the singlet state [the last term of Eq. (19)], so that its coefficient is a correction to the parameter $a\Lambda$,

$$\Delta(a\Lambda) = \frac{2A^{(2)}[b^{(2)} + c^{(2)}]}{E_{\text{singlet}}^0 - E_{\text{triplet}}^0}. \quad (35)$$

The third term of Eq. (33) gives a very small correction to the electric quadrupole interaction which can be ignored. The parameters $A^{(2)}$ are defined by Eqs. (22), (24), and (26) for the Δ , Φ , and Π states; the energy denominators can be calculated from the observed energies of Fig. 1, and the hyperfine parameters are simply the differences of the one-electron parameters for the two unpaired electrons.

We can now apply Eq. (35) to the $a^1\Delta$ and $f^1\Phi$ states (the $e^1\Pi$ state has already been deperturbed). For the $\sigma\delta$ $a^1\Delta$ state, $[b^{(2)} + c^{(2)}]$ becomes $(-b_\sigma + c_\delta)$. If we neglect the small dipolar constant c_δ and take b_σ as 0.0864 cm^{-1} from Ref. 4, Eq. (35) gives

$$\Delta(a\Lambda) = \frac{2 \times 460.2 \times -0.0864}{4706.7} = -0.0169 \text{ cm}^{-1}. \quad (36)$$

This means that the apparent $a\Lambda$ parameter for the $a^1\Delta$ state has been lowered by 0.0169 cm^{-1} . Adding this amount to the measured $a\Lambda$ constant for $a^1\Delta$ given in Table VI, we obtain the deperturbed value as $(0.0054 + 0.0169) = 0.0223 \text{ cm}^{-1}$. This number is within about 10% of the $a\Lambda$ value for the $^3\Delta$ state, 0.02485 cm^{-1} ; in other words the agreement is at the level expected in the single configuration model.

The second-order interaction between the $f^1\Phi$ and $B^3\Phi$ states from the $\delta\pi$ configuration is considerably smaller than that for the Δ states, since the spin-orbit matrix element is not so large [see Eq. (29)]. If we take the second-order hyperfine constants $b^{(2)}$ and $c^{(2)}$ as those for the $\delta\pi^1\Pi/{}^3\Pi$ complex, from Table V, $A^{(2)}$ from Eq. (29), and $\Delta E^0(^1\Phi - ^3\Phi)$ from Fig. 1, Eq. (35) gives the correction to the $a\Lambda$ parameter for the $^1\Phi$ state:

$$\begin{aligned} \Delta(a\Lambda) &= \frac{2 \times 154.9(-0.0949 + 0.0126)}{5360.5} \\ &= -0.0047 \text{ cm}^{-1}. \end{aligned} \quad (37)$$

Adding this correction to the apparent $a\Lambda$ value (0.0369 cm^{-1}), we find the deperturbed $a\Lambda$ constant for $f^1\Phi$ to be 0.0416 cm^{-1} , which is close to the reported value for the $B^3\Phi$ state (0.0401 cm^{-1} , Table VII).

The value of $\Delta(a\Lambda)$ in Eq. (37) is probably too large, because the corresponding correction in the $B^3\Phi$ state, $a\Lambda - h(\Sigma=0)$, is only -0.0010 cm^{-1} .⁴ If this value is used in Eq. (37), $b^{(2)} + c^{(2)}$ is given as -0.0173 cm^{-1} , which seems more reasonable as it is then similar to the diagonal hyperfine combination, $(b+c)(^3\Phi) = -0.0232 \text{ cm}^{-1}$. The lower value for $\Delta(a\Lambda)$ leads to the quantity $a\Lambda(^1\Phi) = 0.0379 \text{ cm}^{-1}$, about 95% of the corresponding triplet state parameter.

The one-electron spin-orbit and hyperfine parameters are both proportional to the expectation value $\langle r_i^{-3} \rangle_{nl}$, so that the deperturbed values should be in a constant ratio.²² Specifically, the ratio should be

$$\frac{a_{\text{spin-orbit}}}{a_{\text{hyperfine}}} = \frac{g\mu_B Z_{\text{eff}}}{2g_N\mu_N}, \quad (38)$$

where Z_{eff} is the effective nuclear charge in the Coulomb potential for the spin-orbit interaction. The one-electron spin-orbit parameters are given in Table VIII, while the hyperfine parameters are

$$\begin{aligned} 2a_\delta &= 0.02485 \text{ cm}^{-1} \text{ (from } X^3\Delta) \\ &\text{or } 0.0257 \text{ cm}^{-1} \text{ (from } B^3\Phi \text{ and } C^3\Pi), \end{aligned} \quad (39)$$

$$a_\pi = 0.0144. \quad (40)$$

The ratios $a_{\text{spin-orbit}}/a_{\text{hyperfine}}$ for these three sets of quantities (divided by 10^4) are 3.61 and 3.93, for the δ electron, and 4.21, for the π electron. The parameters themselves will not be the same for the $3d\delta$ and $3d\pi$ electrons, even though $\langle r_i^{-3} \rangle_{nl}$ does not depend on m_l , because the π electron is not in a pure $3d\pi$ molecular orbital; however the ratios should take this into account. The agreement appears to be very satisfactory, though the fact that it is not perfect suggests that higher order effects caused by other electronic states could be important in determining the exact values of the parameters. It will be instructive to try to model these by *ab initio* methods.

C. The Fermi contact and dipolar interactions

The Fermi contact interaction is a measure of the unpaired electron spin density at the spinning nucleus. Only unpaired σ electrons in molecular orbitals derived from metal s atomic orbitals have nonzero spin density at the nucleus; such electrons give rise to positive Fermi contact parameters, assuming that the nuclear magnetic moments are themselves positive. If there are no unpaired electrons in σ molecular orbitals the Fermi contact parameter will be zero, though in practice a small negative value is usually found because of spin polarization.¹⁵ These are the reasons why the Fermi contact parameter for the $\sigma\delta$ $X^3\Delta$ state is positive, while that for the $\delta\pi$ $B^3\Phi$ state is negative, as shown in Table VII.

A detailed discussion of the Fermi contact and dipolar parameters for the $X^3\Delta$ and $B^3\Phi$ states was given in Ref. 4. For the $C^3\Pi$ state, the diagonal Fermi contact parameter b is essentially zero, as was indicated in Sec. V B. The parameter $b^{(2)}$ in the matrix element $\langle ^1\Pi | H | ^3\Pi \rangle$ was determined to be $-0.0949 \pm 0.0008 \text{ cm}^{-1}$. Since $b^{(2)}$ appears only in the off-diagonal elements its sign cannot be obtained, although the least squares results show that it is opposite to that of $A^{(2)}$; if $A^{(2)}$ is taken to be positive, from Eq. (26), $b^{(2)}$ must be negative. The negative sign is consistent with its origin being spin polarization in the configuration $\delta\pi$, with no $\sigma\sigma$ unpaired electrons present. The magnitude of $b^{(2)}$ is almost certainly too high, since it is about twice as large as the diagonal parameter in the $\sigma\delta$ ground state. We suspect that the lack of data on the J

dependence of the hyperfine splitting in the $^1\Pi$ state means that there are still correlations between the off-diagonal hyperfine parameters in the least squares results. Although the parameter $b^{(2)}$ fits the available data, it seems to be too large by a factor of 4, as we have just discussed.

The diagonal and off-diagonal parameters c and $c^{(2)}$, which describe the dipolar hyperfine effects in the $^1\Pi/{}^3\Pi$ complex, are related to the one-electron parameters c_δ and c_π by

$$c = \frac{1}{2}(c_\delta + c_\pi), \quad c^{(2)} = \frac{1}{2}(c_\delta - c_\pi). \quad (41)$$

From the values of c and $c^{(2)}$ given in Table V we obtain

$$c_\delta = 0.0184 \text{ cm}^{-1}, \quad c_\pi = -0.0068 \text{ cm}^{-1}, \quad (42)$$

taking the sign of $c^{(2)}$ to be the same as that of $A^{(2)}$ from the least squares results. The opposite signs of the dipolar parameters for the δ and π electrons can be understood from the microscopic expression for the dipolar parameter:

$$c = (\mu_0/4\pi\hbar c) (3g\mu_B g_N \mu_N/2) \left(\frac{1}{2S} \right) \times \sum_i \langle 3 \cos^2 \theta_i - 1 \rangle_{ik} \langle r_i^{-3} \rangle_{nl}, \quad (43)$$

where the angular factors for the $d\delta$ and $d\pi$ electrons are²³

$$\langle 3 \cos^2 \theta - 1 \rangle_{d\delta} = -\frac{4}{7}, \quad \langle 3 \cos^2 \theta - 1 \rangle_{d\pi} = \frac{2}{7}. \quad (44)$$

We do not press this analysis further because it is not clear that the deperturbation has fully broken the least-squares correlation between the parameters $b^{(2)}$ and $c^{(2)}$, which can be distinguished in principle because they have different J dependences for their matrix elements.

To summarize the conclusions, we now have spin-orbit and hyperfine data for all the states from the two low-lying configurations $\sigma\delta$ and $\delta\pi$, and can rationalize them with some success in terms of one-electron spin-orbit and hyperfine parameters in the single configuration approximation. The measurement of the hyperfine parameters of the $a^1\Delta$ and $f^1\Phi$ states has provided direct confirmation that second-order spin-orbit/Fermi contact interaction between the singlet and triplet states from the same electron configuration makes substantial corrections to the coefficients of the $\mathbf{I} \cdot \mathbf{L}$ magnetic hyperfine interaction; the corrections are equal and opposite in the singlet and triplet states, and are the hyperfine equivalent of the distortion of the spin-orbit intervals in a triplet state by the singlet state from the same configuration. It is clearly necessary to take account of this effect when reporting the hyperfine parameters for any open shell molecules where the Fermi contact or spin-orbit interactions are large; it will be particularly insidious in singlet states where the corresponding triplet state has not been studied in detail.

IX. NEW ELECTRONIC TRANSITIONS IN THE NEAR INFRARED REGION

Wavelength-resolved fluorescence spectroscopy, following laser excitation of selected transitions, is a powerful

technique for studying low-lying electronic states that are accessible only with difficulty by absorption methods.

Four excited electronic states of NbN can be easily populated by cw laser methods, namely the $B^3\Phi$, $C^3\Pi$, $e^1\Pi$, and $f^1\Phi$ states. This section describes emission spectra in the region 12 000–13 000 cm^{-1} resulting from such excitations. Nothing new appears when the $B^3\Phi$ state is excited, but two new electronic transitions were found following laser excitation of the $C^3\Pi$ state, two more were given by the $e^1\Pi$ state, and a fifth came from the excited $f^1\Phi$ state.

A. The $C^3\Pi-A^3\Sigma^-$ and $C^3\Pi-a^1\Delta$ transitions

Transitions from the $C^3\Pi$ state to the $\delta^2 A^3\Sigma^-$ and $\sigma\delta a^1\Delta$ states have been observed near 8100 Å in wavelength-resolved fluorescence experiments following excitation of the $C-X$ transition. Figures 14 and 15 show examples of the spectra. The $C^3\Pi-A^3\Sigma^-$ patterns are unusual and show that the $\Omega=0^+$ component of the $^3\Sigma^-$ state lies nearly 500 cm^{-1} below $\Omega=1$. In Fig. 14(a) the laser excites the overlapping $P(9)$ and $Q(38)$ lines of the $C^3\Pi_2-X^3\Delta_3$ subband; two sets of R , Q , and P lines are observed. The line intensities show that this is a $\Delta\Omega=+1$ transition, in other words $^3\Pi_2-^3\Sigma_1^-$. The doubling of the $R(37)$, $Q(38)$, and $P(39)$ lines in Fig. 14(a) results from the Ω doubling in the case (a) $^3\Sigma_1^-$ state; the laser populates both Λ -doubling components of $^3\Pi_2$, $J'=38$, which then emit to the two lower state Ω components. The Ω doubling in $^3\Sigma_1^-$ increases linearly with $J(J+1)$ and is not resolved at low J , as in the $R(7)$, $Q(8)$, and $P(9)$ lines. Excitation of the $C^3\Pi_{0-}X^3\Delta_1(0,0)$ $Q(28)$ line produces the spectrum shown in Fig 14(b); only one Λ component of the upper state is populated, so that no line doubling is seen. The other Λ component can be seen as the collision-induced Q branch 6 cm^{-1} to the red of the excited line [see Eq. (3)]. It was the observation of the Ω doubling of the $A^3\Sigma_1^-$ state that allowed us to assign the e, f parities of the various components. The only expected low-lying $^3\Sigma$ state is $\delta^2 A^3\Sigma^-$; its $\Omega=0$ component is therefore 0_e^+ . Now, if the $\Omega=0^+$ component has e parity and lies below the $\Omega=1$ component, the Ω doubling of the latter will be in the sense e above f , as a result of the spin uncoupling. The spacing of the R , Q , and P lines in Fig. 14(b) then immediately identifies them as R_{ff} , Q_{fe} , and P_{ff} lines, showing that the upper state is $^3\Pi_{0f}$.

Excitation of the $C^3\Pi_1$ component, which is out of place as a result of the $^1\Pi/{}^3\Pi$ interaction described above, gives spectra such as that shown in Fig. 15. The high frequency feature is the $C^3\Pi_1-A^3\Sigma_{0+}^-$ subband, by chance nearly at the same position as the $C^3\Pi_{0-}A^3\Sigma_1^-$ subband, while 85 cm^{-1} to the red is another band, identifiable from the line strengths as an $\Omega=1-2$ transition. The only low-lying $\Omega=2$ state has to be the $\sigma\delta a^1\Delta$ state, so that this measurement gave us its absolute energy. The great strength of the $^3\Pi_1-^1\Delta_2$ intercombination band relative to the spin-allowed $^3\Pi_1-^3\Sigma_{0+}^-$ subband is an indication of the mixing of singlet and triplet character in the $^1\Pi/{}^3\Pi$ complex.

No high resolution spectra have been obtained for the

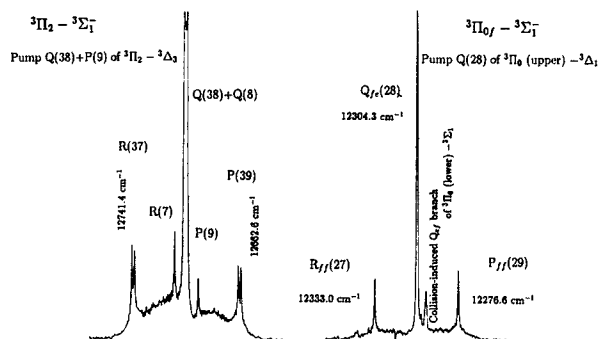


FIG. 14. Wavelength-resolved fluorescence spectra near 8000 Å observed following selective laser excitation of the $C^3\Pi-X^3\Delta$ transition of NbN. (a) the $C^3\Pi_2-A^3\Sigma_1^-$ (0,0) and (b) the $C^3\Pi_{0f}-A^3\Sigma_1^-$ (0,0) subbands.

$C^3\Pi-A^3\Sigma^-$ bands; however we have obtained rotational constants for the $A^3\Sigma^-$ state from dispersed fluorescence spectra following excitation of Q lines of the $C-X$ transition, combined with the $C^3\Pi$ energy levels from the high resolution work. The energy levels of the $^3\Sigma^-$ components were fitted to the simple expression of Eq. (1), and the results are given in Table IX.

B. The $e^1\Pi-a^1\Delta$ and $e^1\Pi-b^1\Sigma^+$ transitions

The $e^1\Pi-a^1\Delta$ transition is quite weak, but dispersed fluorescence can be observed following excitation of the $e^1\Pi$ state. Near 7300 Å lie the $e^1\Pi-a^1\Delta$ and $e^1\Pi-A^3\Sigma_0^+$ systems, which are illustrated in Fig. 16. The spin-allowed $e^1\Pi-a^1\Delta$ transition is stronger than the $e^1\Pi-A^3\Sigma_0^+$ intercombination system, as expected, but the intensity patterns are not exactly the mirror images of Fig. 15, as they should be in the absence of other interactions. The eigenvectors from the deperturbation of the $e^1\Pi/C^3\Pi$ complex predict that the intensity ratio of the allowed and forbidden components should be

$$\frac{I_{\text{spin-allowed}}}{I_{\text{intercombination}}} = 1.16:1. \quad (45)$$

This ratio is roughly what is found in Fig. 15, but in Fig. 16 the ratio is about 6:1. We have no explanation for this effect, although there is no doubt from the line positions that the assignments are correct.

About 650 cm^{-1} to the red of the $e^1\Pi-a^1\Delta$ transition lies another emission from the excited $e^1\Pi$ state. The fluorescence patterns illustrated in Fig. 17 identify it as a $^1\Pi-^1\Sigma^+$ transition. The reasoning is as follows. When the Λ doubling is not resolved in the $e^1\Pi-X^3\Delta_2$ band, the laser excites both parity components of the upper state, and a regular three line (R, Q, P) fluorescence pattern is obtained, as shown in Fig. 17(a); when the Λ doubling is resolved and the laser excites only one of the Λ components of a rotational line, two different fluorescence patterns are obtained: in Fig. 17(b), a single fluorescence line, $Q(36)$, is observed following laser excitation of the lower Λ component of the $R(35)$ line, while in Fig. 17(c) two rotational lines, $R(35)$ and $P(37)$, are observed in the resolved fluorescence following excitation of the upper Λ component of the same rotational line. These fluorescence patterns show that the lower state is nondegenerate, namely a $^1\Sigma$ or $^3\Sigma_0$ state. Since no low-lying $^1\Sigma^-$ state is predicted, and the $A^3\Sigma_0^-$ state has been located a few hundred cm^{-1} below, the new state has to be the $\sigma^2 b^1\Sigma^+$ state, which is expected to lie roughly in this region by analogy with the spectra of TiO and ZrO.^{24,25}

Constants for the $b^1\Sigma^+$ state, derived from the rotational lines of the $e-b$ transition, are given in Table IX, while the line frequencies are listed in the thesis of G.H.

C. The $f^1\Phi-c^1\Gamma$ transition

Laser excitation of the $f^1\Phi-a^1\Delta$ (0,0) band at 17 115 cm^{-1} gave a new electronic transition near 8000 Å in wavelength-resolved fluorescence experiments. This is easily identified as a $^1\Phi-^1\Gamma$ transition from the relative branch intensities, which are illustrated in Fig. 18. The very great intensity of the P branch at low J relative to the R branch is characteristic for a $\Delta\Omega = -1$ transition where Ω is comparatively high. It can be shown quantitatively that the measured intensity ratios of the $R(J-1)$ and $P(J+1)$ lines agree with those calculated for a $^1\Phi-^1\Gamma$ transition. For example, from Fig. 18(b), the intensity ratio $I[P(22)]/I[R(20)]$ is measured to be 1.71, while the Hönl-London factors¹⁰ for an $\Omega=3-4$ transition give the ratio as 1.65.

Rotational constants for the new $^1\Gamma$ state, here called $c^1\Gamma$, were derived by least squares from a number of rotational lines of the $f^1\Phi-c^1\Gamma$ transition. Since accurate rotational constants for the $f^1\Phi$ state are available from sub-Doppler analysis of the $f^1\Phi-a^1\Delta$ (0,0) transition, as reported in Sec. VI, we again fixed the upper state rotational constants to the known values and fitted the line frequencies, using Eq. (1) for the energy levels. The derived rotational constants for the $c^1\Gamma$ state are given in Table IX and the line frequencies are listed in the Ph.D. thesis of G.H.

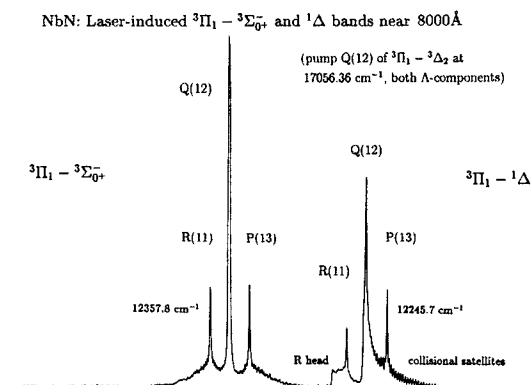


FIG. 15. Wavelength-resolved fluorescence spectra near 8000 Å observed following selective laser excitation of the $C^3\Pi_1-X^3\Delta_2$ transition of NbN. The two transitions observed are the $C^3\Pi_1-A^3\Sigma_0^+$ (0,0) and $C^3\Pi_1-a^1\Delta$ (0,0) subbands.

TABLE IX. Rotational constants from the infrared bands of NbN (in cm^{-1}).^a

Subband	ν_0	B'_{eff}	$10^7 D'_{\text{eff}}$	B''_{eff}	$10^7 D''_{\text{eff}}$	σ
$C^3\Pi_2-A^3\Sigma_1^-$	12 702.15(7)	0.496 19 ^c	5.06 ^c	0.4966(2) ^d	4.0(10) ^d	0.095 ^b
$C^3\Pi_0-A^3\Sigma_1^-$	12 297.82(9)	0.496 47 ^c	5.08 ^c	0.4957(2) ^c	6.0(10) ^c	
$C^3\Pi_1-A^3\Sigma_0^-$	12 759.52(14)	0.495 3 ^c	4.98 ^c	0.4956(12)	1.(19)	0.064
$C^3\Pi_1-a^1\Delta$	12 808.02(8)	0.495 3 ^c	4.98 ^c	0.5079(5)	3.3(63)	0.040
$e^1\Pi-b^1\Sigma^+$	12 994.63(10)	0.494 9 ^f	5.17 ^f	0.4979(5)	-0.11(37)	0.11
$f^1\Phi-c^1\Gamma$	12 394.18(9)	0.495 1 ^g	4.90 ^g	0.4999(10)	5.9(83)	0.31

^aError limits in parentheses are three standard deviations, in units of the last significant figure quoted.

^bCombined fit.

^cValues from Table I, fixed.

^dConstants for $^3\Sigma_{1e}^-$.

^eConstants for $^3\Sigma_{1f}^-$.

^fValues from Table V, fixed.

^gValues from Table VI, fixed.

It is clear that the $c^1\Gamma$ state comes from the configuration δ^2 , from its position 4300 cm^{-1} above $\delta^2 A^3\Sigma^-$. This interval corresponds to the exchange integral $K_{\delta\delta}^4$, which is expected to be in the neighborhood of 4000 cm^{-1} . No other allowed emission transition from $f^1\Phi$ is expected.

X. DISCUSSION AND CONCLUSIONS

The electronic states now known for NbN are summarized in Fig. 1. All of them, except the charge transfer states, which will be described elsewhere, are readily assigned to their electron configurations from the spin-orbit coupling constants and hyperfine parameters. The single configuration approximation is found to hold very well for these states, with the only places where it breaks down being the energy spacings within the $\delta\pi$ configuration and the large second-order spin-orbit splitting of the $\delta^2 A^3\Sigma^-$ state.

The energies of the states from the configuration $\delta\pi$ depend, in the single configuration approximation, on the integrals $K_{\delta\pi}^1$ and $K_{\delta\pi}^3$.²⁶ The separation of the triplet states should be the same as the separation of the singlet states, but with the Λ values reversed, that is

$$E(^3\Pi) - E(^3\Phi) = E(^1\Phi) - E(^1\Pi) = (K^1 - K^3)\delta\pi. \quad (46)$$

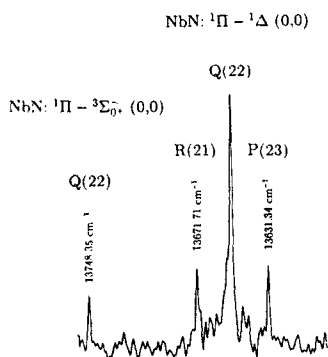


FIG. 16. Weak wavelength-resolved spectra near 7300 Å observed following selective laser excitation of the $e^1\Pi-X^3\Delta_2$ transition of NbN. The features appearing are the Q branch of the $e^1\Pi-A^3\Sigma_0^-(0,0)$ subband and the $e^1\Pi-a^1\Delta(0,0)$ subband.

The observed separations are 1158 cm^{-1} between the triplets, and 4099 cm^{-1} between the singlets, allowing for the second-order spin-orbit effects. It seems that the $e^1\Pi$ state has been pushed down by almost 3000 cm^{-1} from its expected position.

The splitting of the $\delta^2 A^3\Sigma^-$ state is found to be 492.4 cm^{-1} , which is surprisingly large for a second-order spin-orbit effect. The main contribution to this splitting should be from the matrix element $\langle \delta^2 ^1\Sigma^+ | H_{\text{spin-orbit}} | \delta^2 A^3\Sigma^- \rangle$, which is equal to $2a_\delta$ in the single configuration approximation. Now the energies of the three states $^1\Sigma^+$, $^1\Gamma$, and $^3\Sigma^-$ from the δ^2 configuration should be $J^0 + K^4$, J^0 , and $J^0 - K^4$,²⁶ so that it will be a good approximation to assume the $^1\Sigma^+$ state lies as far above the $^1\Gamma$ state as the $^1\Gamma$ state lies above the $^3\Sigma^-$ state; this places the $^1\Sigma^+$ state at $14\,232.9 \text{ cm}^{-1}$. Then, taking the spin-orbit parameter a_δ as 448.56 cm^{-1} (from Table VII), and applying second-order perturbation theory, the splitting of the $A^3\Sigma^-$ state is calculated to be

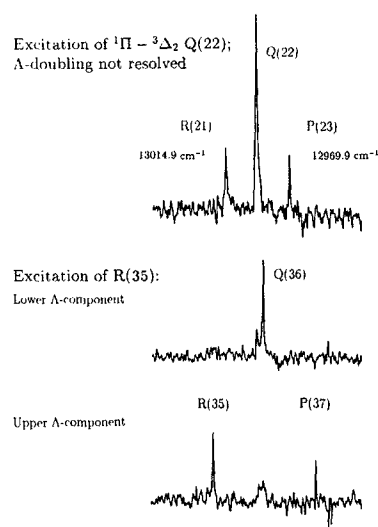


FIG. 17. Wavelength-resolved fluorescence spectra of the $e^1\Pi-b^1\Sigma^+(0,0)$ band of NbN near 7700 Å . For the upper trace the laser excited both Λ components of the $Q(22)$ line of the $e^1\Pi-X^3\Delta_2$ subband, producing R , Q , and P branches; for the lower two traces the laser excited the resolved Λ components of the $R(35)$ line. Since the Kronig symmetry of the lower state is $+$, the parities of the upper state Λ components are identified.

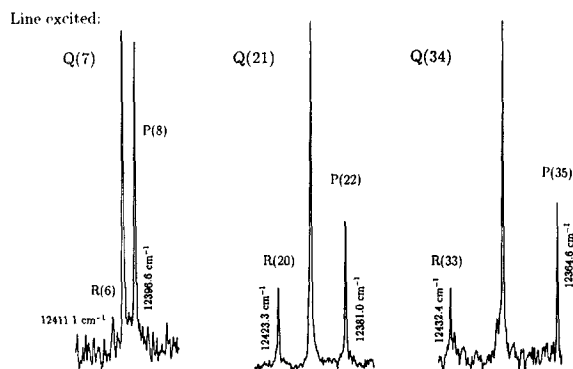


FIG. 18. Wavelength-resolved fluorescence spectra of the $f^1\Phi-c^1\Gamma$ (0,0) band of NbN near 8100 Å, observed following excitation of various Q lines of the $f^1\Phi-a^1\Delta$ (0,0) band. (a) $Q(7)$; (b) $Q(21)$; (c) $Q(34)$.

$$2\lambda(^3\Sigma^-) = \frac{4a_0^2}{\Delta E(^1\Sigma^+ - ^3\Sigma_1^-)} = \frac{4 \times (448.56)^2}{8628.4} = 93.3 \text{ cm}^{-1}. \quad (47)$$

The observed value is over five times larger. The explanation seems to be that there is considerable configuration interaction (CI) between the $\delta^2\ ^1\Sigma^+$ state and the $\sigma^2\ ^1\Sigma^+$ state, which lies at 5862.8 cm^{-1} , just 260 cm^{-1} above $^3\Sigma_1^-$. There is a precedent for this mechanism in the VN spectrum,¹¹ where the $\delta^2\ ^1\Sigma^+$ state interacts with the $\delta\pi\ ^3\Pi$ state, but not as strongly as expected in the single configuration model; the explanation in VN is that CI between the $\delta^2\ ^1\Sigma^+$ and $\sigma^2\ ^1\Sigma^+$ states has reduced the matrix element $\langle \delta\pi\ C^3\Pi_0 | H_{\text{spin-orbit}} | \delta^2\ d^1\Sigma^+ \rangle$. In the NbN case the CI increases the δ^2 character of the $^1\Sigma^+$ state at 5862.8 cm^{-1} , thereby vastly magnifying the second-order splitting in the $\delta^2\ A^3\Sigma^-$ state. This CI is also the reason why the $\delta\pi\ e^1\Pi-\sigma^2\ b^1\Sigma^+$ emission can be observed; the system would be strictly forbidden in its absence, since it implies a two-electron jump where one of the electrons follows $\Delta l = \pm 2$ selection rules. Interestingly, this CI mixing in NbN has been clearly predicted by the *ab initio* calculations of Ref. 27.

The NbN spectrum is otherwise very well behaved; there are no local rotational perturbations in the states described in this paper, and the only irregularities are the spin-orbit effects. These take two forms. One is the familiar depression of the central spin component of a case (a) triplet state by the singlet state from the same configuration; this is a small effect in $B^3\Phi$, rather larger in $X^3\Delta$, and huge in the $C^3\Pi$ state. The $C^3\Pi$ state has its central $\Omega=1$ component pushed 450 cm^{-1} below the $\Omega=0^\pm$ components because the singlet-triplet splitting is particularly small, and the off-diagonal spin-orbit matrix element $\langle ^1\Pi | H_{\text{spin-orbit}} | ^3\Pi_1 \rangle$ is larger than the A parameter of the $^3\Pi$ state. To be exact the $^1\Pi$ state would lie inside the triplet manifold of the $^3\Pi$ state, only 102.6 cm^{-1} above the $^3\Pi_1$ component, if the off-diagonal spin-orbit coupling

could be set to zero. The unusual energy order of the triplet components caused some difficulty in the early stages of the analysis.

The other spin-orbit effect is one that complicates the hyperfine structures of the singlet states and the central components of the triplets. It takes the form of equal and opposite shifts in the hyperfine a parameters of corresponding singlet and triplet states. The mechanism can be understood as a second-order cross term between the spin-orbit and Fermi contact interactions. Evidence for its existence had been reported for the $X^3\Delta$ state in Ref. 4; the new data prove that the interpretation given there was correct, and document the equal and opposite shift in the $a^1\Delta$ state. The corresponding effect in the $^1\Pi/^3\Pi$ complex is very large, because of the size of the spin-orbit element acting between the two states. It even changes the sign of the measured hyperfine a parameter in the $^1\Pi$ state, making it large and negative. This would be a physically unrealistic situation if interpreted literally, which warns that the hyperfine parameters of singlet states in open shell molecules are not straightforward to understand if the corresponding triplet state has not been studied.

The new data in this paper have given a very complete account of the spin and hyperfine structures of the six electronic states making up the electron configurations $(5s\sigma)^1(4d\delta)^1$ and $(4d\delta)^1(4d\pi)^1$. It has been possible to interpret the observations in terms of one-electron parameters for the spin-orbit and electron orbit-nuclear spin interactions. Attempts to obtain one-electron Fermi contact and dipolar hyperfine interaction parameters were less successful because of the limited hyperfine data for the $e^1\Pi$ state. Nevertheless this work represents one of the most complete accounts available for the hyperfine structure of all the states from an electron configuration. With the discovery of three further low-lying states the energy level diagram for NbN is complete up to $15\,000 \text{ cm}^{-1}$, barring the predicted, but as yet unobserved, $\delta^2\ d^1\Sigma^+$ state, which should lie near $14\,000 \text{ cm}^{-1}$.

It is gratifying to see how well the *ab initio* calculations of Ref. 27 reproduce the experimental results. Even the configuration interaction between the $^1\Sigma$ states from the σ^2 and δ^2 configurations, which is important in understanding the spin structure of the $\delta^2\ A^3\Sigma^-$ state, had been noted. In general, the detailed interpretation of the spectrum of a molecule such as NbN will need predictions of the spin-orbit and hyperfine parameters as well as state symmetries and energies; it is hoped that the next generation of *ab initio* programs will include a suitable code for these properties.

ACKNOWLEDGMENTS

We thank Professor T. M. Dunn (University of Michigan) for sending us his unpublished results, and for some stimulating discussions. We thank the Natural Sciences and Engineering Research Council of Canada and the Network of Centres of Excellence in Molecular and Interfacial Dynamics (one of the 15 Networks supported by the Federal Government of Canada) for financial support.

- ¹T. M. Dunn and K. M. Rao, *Nature (London)* **222**, 268 (1969).
- ²E. A. Pazyuk, E. N. Moskvitina, and Y. Y. Kuzyakov, *Spectrosc. Lett.* **19**, 627 (1986).
- ³J.-L. Féménias, C. Athénour, and T. M. Dunn, *J. Chem. Phys.* **63**, 286 (1975).
- ⁴Y. Azuma, J. A. Barry, M. P. J. Lyne, A. J. Merer, J. O. Schröder, and J.-L. Féménias, *J. Chem. Phys.* **91**, 1 (1989).
- ⁵R. A. Frosch and H. M. Foley, *Phys. Rev.* **88**, 1337 (1952).
- ⁶G. Herzberg, *Spectra of Diatomic Molecules*, 2nd ed. (Van Nostrand, Princeton, 1950).
- ⁷M. S. Sorel and A. L. Schawlow, *Opt. Commun.* **5**, 148 (1972).
- ⁸S. Gerstenkorn and P. Luc, *Atlas du Spectre d'Absorption de la Molécule d'Iode* (CNRS, Paris, France, 1978); S. Gerstenkorn and P. Luc, *Rev. Phys. Appl.* **14**, 791 (1979).
- ⁹H. M. Crosswhite, *J. Res. Nat. Bur. Stand.* **79A**, No. 1 (1975).
- ¹⁰H. Hönl and F. London, *Z. Phys.*, **33**, 803 (1925).
- ¹¹W. J. Balfour, A. J. Merer, H. Niki, B. Simard, and P. A. Hackett, *J. Chem. Phys.* **99**, 3288 (1993).
- ¹²J.-L. Féménias, G. Cheval, A. J. Merer, and U. Sassenberg, *J. Mol. Spectrosc.* **124**, 348 (1987).
- ¹³J. M. Brown, E. A. Colbourn, J. K. G. Watson, and F. D. Wayne, *J. Mol. Spectrosc.* **74**, 294 (1979).
- ¹⁴E. Hirota, *High Resolution Spectroscopy of Transient Molecules* (Springer, Berlin, 1985).
- ¹⁵A. Carrington, P. N. Dyer, and D. H. Levy, *J. Chem. Phys.* **47**, 1756 (1967).
- ¹⁶T. M. Dunn (private communication).
- ¹⁷A. J. Merer, U. Sassenberg, J.-L. Féménias, and G. Cheval, *J. Chem. Phys.* **86**, 1219 (1987).
- ¹⁸A. J. Merer, *Annu. Rev. Phys. Chem.* **40**, 407 (1989).
- ¹⁹B. Berno, R. D. Bower, M. Barnes, P. G. Hajigeorgiou, and A. J. Merer (in preparation).
- ²⁰A. S.-C. Cheung and A. J. Merer, *J. Mol. Spectrosc.* **127**, 509 (1988).
- ²¹H. Lefebvre-Brion and R. W. Field, *Perturbations in the Spectra of Diatomic Molecules* (Academic, New York, 1986).
- ²²D. J. Clouthier, G. Huang, A. J. Merer, and E. J. Friedman-Hill, *J. Chem. Phys.* **99**, 6336 (1993).
- ²³T. D. Varberg, R. W. Field, and A. J. Merer, *J. Chem. Phys.* **95**, 1563 (1991).
- ²⁴C. Linton and S. R. Singhal, *J. Mol. Spectrosc.* **51**, 194 (1974).
- ²⁵L. Brewer and D. W. Green, *High Temp. Sci.* **1**, 26 (1969).
- ²⁶J. Raftery, P. R. Scott, and W. G. Richards, *J. Phys. B* **5**, 1293 (1972).
- ²⁷P. W. Langhoff and C. W. Bauschlicher, *J. Mol. Spectrosc.* **143**, 169 (1990).